The effects of nose bluntness on broadband disturbance receptivity in hypersonic flow

Cite as: Phys. Fluids **34**, 054104 (2022); https://doi.org/10.1063/5.0088236
Submitted: 14 February 2022 • Accepted: 18 April 2022 • Accepted Manuscript Online: 19 April 2022 • Published Online: 05 May 2022

Simon He and Xiaolin Zhong

Physics of Fluids ARTICLE scitation.org/journal/phf

The effects of nose bluntness on broadband disturbance receptivity in hypersonic flow

Cite as: Phys. Fluids **34**, 054104 (2022); doi: 10.1063/5.0088236
Submitted: 14 February 2022 · Accepted: 18 April 2022 ·
Published Online: 5 May 2022

Simon He[a] and Xiaolin Zhong[b]

AFFILIATIONS

Mechanical and Aerospace Engineering Department, University of California, Los Angeles, California 90095, USA

[a]Author to whom correspondence should be addressed: simon.he.ucla@gmail.com
[b]xiaolin@seas.ucla.edu. URL: http://cfdhost.seas.ucla.edu

ABSTRACT

While nose bluntness is known to have a large impact on the stability of hypersonic vehicles, its influence on the freestream receptivity process has not been fully characterized for a wide range of conditions. This paper investigates the effects of nose bluntness on the second mode receptivity coefficients and the development of boundary layer disturbances over two 7° half-angle circular blunt cones at Mach 10 after perturbation with broadband freestream pulses of different types. The cones have nose radii of 9.525 mm (case B) and 5.08 mm (case I). Unsteady direct numerical simulation (DNS) and linear stability theory (LST) results compare well and predict stronger second mode growth for case I in all pulse cases. Unsteady DNS also shows variations in extramodal excitation between the cones depending on freestream disturbance type. Spectral receptivity coefficients are generated by decomposing the unsteady DNS data into discrete frequency Fourier modes, which are then corrected with LST N-factors. Fast acoustic disturbances demonstrate minimal variation in receptivity coefficients, while temperature and vorticity disturbances have much higher coefficients in case I. Planar slow acoustic pulses induce stronger disturbances outside of the second mode in case I, resulting in higher peak receptivity coefficients. Results show significant variation in receptivity response based on nose bluntness, pulse geometry, and the type of incident perturbation.

I. INTRODUCTION

In hypersonic flows, the laminar to turbulent transition has been shown to have dramatic effects on the skin friction, surface heating, and overall control of vehicles. Controlling this process is critical to designing the next generation of hypervelocity vehicles.[1–3] Transition in a hypersonic boundary layer is highly complex and governed by several mechanisms. In the case of weak environmental forcing, as assumed in this work, the transitionary process can be broken down into three primary stages: (i) boundary layer receptivity, (ii) linear growth of small amplitude disturbances, and (iii) nonlinear breakdown at finite disturbance amplitudes,[4] though under certain conditions, these steps may be circumvented in a process called bypass transition.[5] Traditional procedures for estimating transition rely on the second step, the linear growth of small amplitude disturbances, which can be modeled and studied using stability analysis tools such as linear stability theory (LST) or the parabolized stability equations (PSE). These stability calculations can be used to predict the relative amplification factor of disturbances in the boundary layer, called the N-factor, which can be correlated with experimental data to estimate transition. This is the eponymous e^N method that has seen the most widespread application.[6,7] While this method is useful for predicting transition within a given set of experimental conditions, it has been criticized for inadequately representing the broadband nature of disturbances in the boundary layer. The e^N method also does not take into account the absolute magnitude of the initial disturbances that may be present in a flow field, which can vary widely between experiments due to environmental conditions. This can, in turn, lead to significant variation in reported transition N-factor thresholds[8] between different experimental facilities. More advanced transition prediction methods that account for these factors have been a topic of interest for quite some time. Mack[9] developed an amplitude method to correlate the broadband disturbance content in the boundary layer for transition. Recent expansions on this methodology by Fedorov and Tumin[10] and Marineau[11] have been proposed to improve the overall accuracy of the predictions and to further refine the amplitude method for engineering application. However, full implementations of the amplitude method require accurate estimates of the initial disturbance amplitudes in the boundary layer. Such data can be taken from experimental correlations, or from high-fidelity receptivity simulations utilizing direct numerical simulation (DNS) such as the one presented in this study.

The receptivity process is the mechanism through which external forcing is converted into disturbances in the boundary layer. The modulation and growth of these perturbations can eventually trip the flow and cause transition. Due to its potential impact on transition, the receptivity to freestream disturbances has been rigorously investigated for a variety of geometries in hypersonic flows, including flat plates[4,12–18] and cones.[19–27] For flat plates, it was found that freestream acoustic, entropy, and vorticity disturbances were able to induce both continuous and discrete instability modes in the boundary layer, though acoustic disturbances were most able to excite the primary second mode instability.[4,15] Similar findings were also found for cones with acoustic disturbances inducing much stronger second mode growth compared to entropy and vorticity disturbances.[19,21] However, the relative strength of the boundary layer perturbations resulting from the entropy and vorticity disturbances was found to be much stronger in cones than that in the flat plate cases, indicating potentially different receptivity paths for these freestream disturbance types.[22] Kara *et al.*[24] studied the effects of nose bluntness in cones on the receptivity to discrete slow acoustic waves. They found that large bluntnesses strongly attenuated initial second mode amplitudes. Wan *et al.*[26] and Chen *et al.*[28] further investigated the receptivity mechanism of planar slow acoustic waves over blunt cones and wedges to further characterize the development of instability modes. They found that acoustic waves excited fast acoustic boundary layer modes along with entropy layer modes upstream on the geometry. The fast acoustic modes were found to significantly dampen while the entropy layer disturbances grew to dominate and force more amplified downstream instabilities.

A large majority of these prior receptivity studies have focused on discrete frequency disturbances. Environmental perturbations in experimental and flight conditions, however, are generally broadband in nature.[29] This has motivated recent receptivity studies to begin incorporating more multi-frequency and broadband freestream disturbance models. Zhong[30] and Balakumar and Chou[23] used selected combinations of discrete frequency continuously radiating waves to approximate multi-frequency freestream disturbances. Zhong attempted to track transition reversal effects using the broadband disturbance but was unable to observe it in his test case. Balakumar and Chou showed that packets of multiple discrete frequency disturbances could be used to improve the accuracy of transition prediction in sharp cones, though their methodology was less accurate for their blunter test cases. Motivated by laser perturbation experiments from Purdue by Wheaton *et al.*[31] and Chou *et al.*,[32,33] Huang and Zhong[22] simulated hotspot disturbances using freestream Gaussian pulses. They found that this pulse model could excite significant modal instabilities while providing broadband, analytical disturbances in the freestream. Similar impulsive acoustic disturbances have also previously been experimentally studied using spark-inducers.[34] Chuvakhov *et al.*[35] simulated the receptivity to small particulates in supersonic flows to investigate the potential effects of atmospheric or experimental dust particulates. They demonstrated broadband excitation of both continuous and discrete instability modes and showed that particulates could excite wavepackets of amplified modal instabilities. Browne *et al.*[36] used similar methodologies and investigated the receptivity over a wedge and flat plate to different particle impingement locations. While these models also offer sources of broadband excitation, they do not encompass the wide range of other potential freestream disturbance types that may be present in experimental or flight conditions. He and Zhong[27] simulated the receptivity of a blunt cone to a variety of finite and planar freestream pulses consisting of acoustic, temperature, and vorticity disturbances. They similarly found that slow acoustic disturbances generated the strongest second mode receptivity response and also showed that while planar fast acoustic pulses induced weak second mode growth, they were highly capable of exciting disturbance bands outside of the primary second mode. This highly broadband response to the planar fast acoustic pulse was not previously observed in other receptivity studies and seems to be a consequence of the broadband freestream disturbance itself. This is indicative of the importance of considering fully broadband incident disturbances to fully capture all of the flow features that may be present in an experimental environment.

Recent investigations of stochastic freestream perturbations have also been made to more closely match the nature of disturbances found in actual flight[37] as well as to account for the limited availability of environmental disturbance data[18,38] for some configurations. Egorov *et al.*[37] investigated the impact of phase coherence in freestream disturbances to determine the potential impact on receptivity coefficients. In this case, coherence refers to consistent phase relations in the disturbance spectra of the incident perturbation. Incoherent disturbances introduce forcing with the randomized phase into the flow. Egorov *et al.*[37] asserts that incoherent disturbances, such as from random incident acoustic waves or distributed surface roughness, are more capable of inducing instability than coherent disturbances. Hader and Fasel[39] used randomized pressure perturbations to investigate the nonlinear breakdown over cones and showed that they presented similar breakdown mechanisms to their previous results with controlled disturbances. Goparaju *et al.*[18] expanded on this and investigated the receptivity of flat plates of different bluntnesses to stochastic pressure disturbances in an attempt to explain the transition reversal phenomenon observed in geometries with large leading-edge bluntness. They observed significant excitation in the entropy layer of their flat plate case along with a reversal in the growth rate. Further investigations on the effects of phase coherence will be necessary to further refine our understanding of receptivity in hypersonic flows.

Most practical designs for hypersonic vehicles include some form of nose bluntness, which greatly complicates the stability profile of the flow due to the introduction of features such as distinct entropy layers and increased sensitivity to local surface roughness. Small to moderate nose bluntness has been shown experimentally and numerically to slow second mode growth and delay transition. However, extremely large nose bluntnesses have also been observed to result in a reversal in this phenomenon, causing transition much earlier than expected.[40–42] Studies have shown that the second mode is unlikely to be the primary driver of this early transition, as it is still stabilized by the large nose bluntness, and the true cause of the reversal phenomenon remains an open question.[24,43] Recent efforts have attempted to investigate the impact of non-modal disturbance growth on the transition reversal phenomenon observed at large bluntnesses as well as on the reduced stabilizing effect of intermediate nose bluntness. Reshotko and Tumin[5,44–46] proposed that transient growth of locally stable, non-orthogonal instability modes could lead to algebraically amplified disturbances that can induce early transition in the bypass mechanism mentioned previously. Paredes *et al.*[47–49] investigated the non-modal growth of disturbances near the frustum of blunt cones to attempt to

explain the reversal phenomenon. Similar to Goparaju *et al.*,[18] they found that traveling disturbances in the entropy layer experienced non-modal excitation and could, under certain circumstances, replicate the reversal observed in the experiment.

These previous studies demonstrate that both nose bluntness and freestream receptivity are important for the development of instabilities in hypersonic boundary layers. However, the coupling of these two effects has not yet been extensively investigated, especially in the case of broadband disturbances, which are much more representative of experimental environments. Prior work in this line is found in the aforementioned studies by Kara *et al.*[24] and Goparaju *et al.*[18] The receptivity study by Kara *et al.* considered a range of sharp and blunt cones and demonstrated substantial weakening of second mode receptivity coefficients in response to larger nose bluntness. However, their study primarily focused on the receptivity to single frequency, discrete slow acoustic waves in the freestream. In order to further generalize receptivity data, and capture the full envelope of potential conditions in flight and experiment; the scope of disturbances must be expanded to include broadband freestream perturbations of many types. While Goparaju *et al.* investigated the receptivity of flat plates to broadband stochastic freestream perturbations, their work also primarily focused on only the receptivity to acoustic disturbances. Additionally, although they tracked the development of instability structures in detail, Goparaju *et al.* did not report receptivity coefficient data that are necessary to fully characterize the receptivity response and to utilize more advanced amplitude methods. Intrinsic differences in receptivity mechanisms between flat plate and cone geometries also necessitate additional consideration.[22] As such, in this paper, we aim to investigate the coupled effects of nose bluntness and broadband freestream pulse receptivity in a selection of blunt cones by calculating and contrasting their receptivity coefficients and phase angle spectra. General spectral disturbance profiles are also compared between the blunt cone cases. Particularly, spectral receptivity coefficients such as those from He and Zhong[27] are studied. These receptivity data are unique in that they produce coefficients for a wide range of second mode frequencies, and similar results are not widely published. Such data can directly replace empirical correlations in the absence of reliable experimental data and can potentially be generalized to similar geometric cases for amplitude method implementations like Marineau's.[11] The following analysis encompasses unsteady direct numerical simulation (DNS) and LST stability analysis and provides high fidelity data on two blunt cones based on AEDC wind tunnel 9 experiments by Marineau *et al.*[50] The results of this study and other similar work will be necessary to produce updated receptivity databases that are pivotal for the development and direct application of more advanced transition prediction schemes.

II. SIMULATION CONDITIONS

The current study compares the receptivity response of two blunt cones with 7° half-angles at Mach 10 to freestream fast acoustic, slow acoustic, temperature, and vorticity disturbances. The pulses are composed of two geometries: a finite spherical geometry that isolates forcing to the nose regions of the cones and a planar pulse configuration that also generates additional instabilities downstream on the cones. The incident perturbations are modeled as Gaussian pulses in the freestream, which result in broadband frequency spectra. The DNS simulations use 240 points in the wall-normal direction and roughly five points per millimeter on the surfaces of the cones in the streamwise direction. For the axisymmetric simulations here, four points are used in the periodic spanwise direction, although only one point is directly calculated at each time step. The flow conditions for this study are summarized in Table I and are based on the tunnel conditions reported by Marineau *et al.*[50] for runs 3746 and 3752. Case B refers to the blunter 9.525 mm nose radius cone from run 3752, while case I, in this study, refers to the 5.08 mm cone in run 3746. The Prandtl number, specific gas ratio, and gas constant in the simulations are set at $Pr = 0.72$, $\gamma = 1.4$, and $R = 296.8\,J/(kg \cdot K)$, respectively. Data for case B and its corresponding unsteady results are reproduced from Ref. 27, while the data for case I are new. What follows is a comparative study on the impact of nose bluntness to the broadband receptivity over blunt cone geometries.

The DNS code used in this study utilizes a shock-fitting formulation with the parameters in Table I defining the freestream conditions upstream of the shock formed over the body. The viscosity used here was calculated using Sutherland's law, while Marineau *et al.*[50] instead used curve fits of experimental data. This leads to approximately a 10%–12% increase in the calculated freestream unit Reynolds number in this study compared to those reported by Marineau, *et al.* in both mean flows.

III. NUMERICAL METHODS AND DISTURBANCE MODEL

A. DNS

The numerical method of the DNS code is summarized here for clarity, and the reader may refer to Zhong[51] for more extensive details on the algorithm. The receptivity simulations investigated in this study assume calorically perfect gas behavior for molecular nitrogen in the flow field based on the low freestream stagnation enthalpy reported in Table I and the tunnel conditions reported by Marineau *et al.*[50] The three-dimensional conservative Navier–Stokes system consists of a single species mass conservation equation, three-momentum conservation equations, and the energy equation. In the vector form, these equations are written as

$$\frac{\partial U}{\partial t} + \frac{\partial F_j}{\partial x_j} + \frac{\partial G_j}{\partial x_j} = 0 \quad (j = 1, 2, 3), \tag{1}$$

where U is the state vector of conserved quantities, F_j is the invsicid flux vector, and G_j is the viscous flux vector. The j indices denote curvilinear coordinates in the streamwise, surface normal, and azimuthal directions about the cone. The physical domain in the code is defined

TABLE I. Freestream flow conditions for DNS simulations.

Case	R_n, mm	M_∞	$h_{0,\infty}$, MJ/kg	ρ_∞, kg/m^3	p_∞, kPa	T_∞, K	$T_w/T_{0,\infty}$	$Re/m\,(1E6/m)$
B (3752)	9.525	9.79	1.07	0.0427	0.65	51.0	0.3	18.95
I (3746)	5.080	9.81	1.06	0.0422	0.64	50.8	0.3	19.11

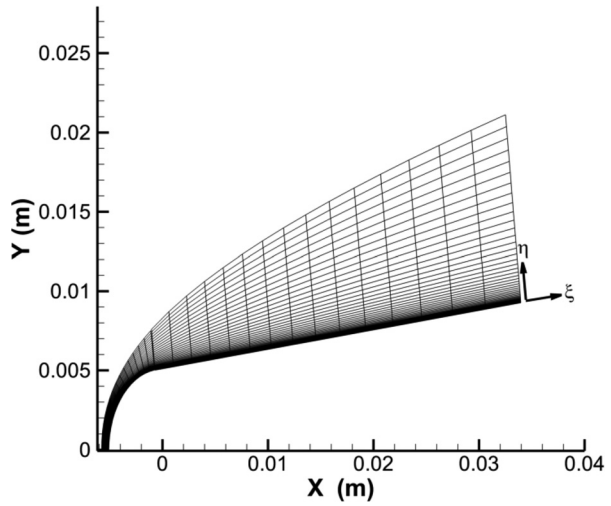

FIG. 1. Schematic of grids near the nose/frustum region of a cone. Grid density is coarsened for clarity.

by these curvilinear grids, which match the curvature of the cone geometry, as shown in the schematic diagram in Fig. 1. The conservative vector U is composed of five conservative flow variables for mass, momentum, and energy. In the shock fitting code, both the shock itself and the surface of the cone are treated as computational boundaries for the grid. Stretching concentrates grid lines near the cone surface so as to provide sufficient resolution to accurately capture boundary layer disturbances.

A low-dissipation, fifth-order upwinded stencil is used for the inviscid fluxes while a sixth-order central stencil is used for the viscous fluxes. The location of the shock boundary is also solved for in the shock-fitting algorithm. Rankine–Hugoniot relations across the shock and characteristic relations behind the shock are utilized to determine flow conditions immediately behind the shock. Isothermal and viscous boundary conditions are imposed at the cone surface, and the wall temperature is fixed based on the conditions as reported in Table I. High order extrapolation is utilized at the domain outlet. Finally, the solution is advanced in time using a low-storage first-order explicit Runge–Kutta method from Williamson.[52]

B. LST

The Linear Stability Theory (LST) implementation used in this study was originally developed and verified by Ma and Zhong.[4,13,14] The LST relations are derived by linearizing the governing Navier–Stokes equations in Eq. (1). First, the instantaneous flow is decomposed into a mean and fluctuating component $q = \bar{q} + q'$ and reintroduced into the governing equations. Since the steady mean flow component is assumed to satisfy the governing equations, it can be subtracted out. A quasi-parallel assumption is also applied such that remaining mean flow terms are functions of y only. To linearize the equations, disturbances are assumed to be small enough such that quadratic and higher order perturbation terms can be removed. A normal mode solution in the form of $q' = \hat{q}(y)\exp[i(\alpha x + \beta z - \omega t)]$ is then introduced, where ω is the circular frequency of the disturbance and α and β are the spatial wavenumbers corresponding to the streamwise and spanwise directions. For a spatial stability analysis the circular frequency of a given disturbance, ω, is manually set while α is complex and must be solved for. This results in the dispersion relation $\alpha = \Omega(\omega, \beta)$. Additionally, β is set to 0 since the disturbances are assumed to be two-dimensional for this study. The complex spatial wavenumber α can be written in terms of its real and complex components as $\alpha = \alpha_r + i\alpha_i$, where $-\alpha_i$ is the growth rate of the disturbance. Substituting in the normal mode reduces the problem to a coupled set of 5 ordinary differential equations in the following form:

$$\left(\mathbf{A}\frac{d^2}{dy^2} + \mathbf{B}\frac{d}{dy} + \mathbf{C}\right)\vec{\phi} = \vec{0}. \tag{2}$$

The terms $\vec{\phi} = [\hat{u}, \hat{v}, \hat{P}, \hat{T}, \hat{w}]^T$ and **A**, **B**, and **C** are complex square matrices of size 5. The linearization applied here results in a boundary value problem where the derivative operators can be discretized and the system can be numerically solved. The boundary conditions for Eq. (2) are defined as

$$y = 0; \quad \phi_1 = \phi_2 = \phi_3 = \phi_4 = \phi_5 = 0, \tag{3}$$

$$y \to \infty; \quad \phi_1, \phi_2, \phi_3, \phi_4, \phi_5 \to 0. \tag{4}$$

This linearized system of equations is solved using a multi-domain spectral method based on Malik's[53] where the converged mean flow from the steady DNS is used as the input to the LST system.

The resulting LST growth rates can be integrated in the streamwise direction to provide the spatial amplification ratio (or N-factor) of different discrete disturbance frequencies. This N-factor is defined as

$$e^{N(s^*,f)} = \frac{A(s^*,f)}{A_0(f)} = \exp\left[\int_{s_0^*}^{s^*} -\alpha_i(s^*,f)ds^*\right]. \tag{5}$$

Here, $A(s^*,f)$ is the spectral amplitude density at position s^* for the disturbance, $A_0(f)$ is the initial amplitude density at the branch I neutral point s_0^*, and α_i is again the spatial amplification rate (growth rate) obtained from LST.

C. Freestream disturbance model

The stability of the two cone geometries is also studied using unsteady DNS simulations. Freestream pulses composed of fast acoustic, slow acoustic, temperature, and vorticity disturbances with broadband frequency spectra are used to perturb the mean flow. Two pulse geometries are utilized: finite spherical pulses, which isolate disturbances upstream on the cone, and planar pulses, which also force the flow downstream on the cone. Since the shock is treated as a computational boundary in the simulations, these pulses can be analytically represented in the freestream by the following equation, with the input parameters for the pulses listed in Table II:

TABLE II. Gaussian pulse parameters for unsteady DNS.

Case	Pulse geometry	ϵM_∞	σ	x_0, m
B (3752)	Finite spherical	5×10^{-4}	1×10^{-3}	−0.02
B (3752)	Planar	1×10^{-6}	1×10^{-3}	−0.02
I (3746)	Finite spherical	1×10^{-6}	1×10^{-3}	−0.02
I (3746)	Planar	1×10^{-8}	1×10^{-3}	−0.02

$$q(x,y,z,t) = |q'|_\infty \exp\left(-\frac{(R_c)^2}{2\sigma^2}\right) + q_\infty. \quad (6)$$

The term q is a stand in for the perturbation variables for density, pressure, velocity, and entropy. Similarly, $|q'|_\infty$ is a stand in for the peak freestream perturbation amplitudes of these variables $|\rho'|_\infty$, $|P'|_\infty$, $|u'|_\infty$, $|v'|_\infty$, and $|s'|_\infty$ as defined by the dispersion relations in Eqs. (7)–(10). The brackets utilized here are not indicative of absolute values or norms of the particular perturbation variables, and the ∞ subscript denotes that the perturbations originate from the freestream.

A freestream fast acoustic disturbance is defined using the following relation:

$$|\rho'|_\infty = \frac{|P'|_\infty}{\gamma} = |u'|_\infty M_\infty = \epsilon M_\infty, \quad |s'|_\infty = |v'|_\infty = 0. \quad (7)$$

A slow acoustic disturbance in the freestream is governed by a very similar dispersion relation,

$$|\rho'|_\infty = \frac{|P'|_\infty}{\gamma} = -|u'|_\infty M_\infty = \epsilon M_\infty, \quad |s'|_\infty = |v'|_\infty = 0. \quad (8)$$

A freestream entropy disturbance is described by

$$|\rho'|_\infty = -|s'|_\infty = \epsilon M_\infty, \quad |u'|_\infty = |v'|_\infty = |p'|_\infty = 0. \quad (9)$$

A freestream vorticity disturbance is described by

$$|v'|_\infty M_\infty = \epsilon M_\infty, \quad |u'|_\infty = |p'|_\infty = |s'|_\infty = 0. \quad (10)$$

The ϵM_∞ variable prescribed in Table II governs the relative peak disturbance amplitude of the freestream pulse and is chosen to ensure that boundary layer disturbances remain linear. Since the receptivity response to the planar pulses was expected to be much stronger than that for the finite spherical pulses, the amplitude parameter ϵM_∞ was reduced for these cases. These peak amplitudes were further reduced for case I due to the stronger expected second mode response. The variable σ controls both the spatial width of the pulse and the frequency bandwidth of the disturbance. This parameter was chosen to encompass significant freestream disturbances at frequencies of up to 600 kHz in order to ensure the excitation of the primary modal instabilities predicted by LST and resulted in a pulse radius of approximately 3 mm. The term R_c refers to the radial distance from the center of the pulse to a point (x, y, z) in the flow field.

For the finite, spherical pulses, this distance R_c is measured in all three spatial dimensions, while for planar pulses only, the streamwise x-distance from the pulse center is taken into account. For both geometries, the pulse is advected in the streamwise direction by $x_{pulse} = x_0 + C_\infty t$, where C_∞ is the disturbance speed in the freestream. These speeds are defined as $C_\infty = U_\infty + a_\infty$ for fast acoustic disturbances, $C_\infty = U_\infty - a_\infty$ for slow acoustic disturbances, and $C_\infty = U_\infty$ for entropy/vorticity disturbances. The pulse width term σ is scaled by $1 + 1/M_\infty$ for a fast acoustic disturbance and by $1 - 1/M_\infty$ for a slow acoustic disturbance to ensure uniform frequency spectra in all of the freestream pulses.

D. Boundary layer receptivity

The spectral disturbance content of the boundary layer disturbances is analyzed through the use of Fourier decomposition. The time-dependent perturbation variables can be expressed in terms of their Fourier spectral components, which are obtained through a Fast Fourier Transform (FFT),

$$h(t_k) \equiv h_k \approx \sum_{n=0}^{N-1} H(f_n) e^{-2\pi i f_n t_k}, \quad (11)$$

where $H(f_n)$ describes a frequency space Fourier coefficient that corresponds to f_n, the nth discretized frequency. N total collocation points are used to discretize the time-dependent function $h(t_k)$ in Fourier space.

Since we are primarily interested in acoustic instabilities in this study, the variable $h(t_k)$ is populated with local surface pressure perturbations. The complex components of $H(f_n)$ correspond to the phase angle of the surface pressure perturbation through the following relation:

$$\phi_n = \tan^{-1}\left(\frac{Im(H(f_n))}{Re(H(f_n))}\right), \quad (12)$$

and $|H(f_n)|$ defines the amplitude of the surface pressure perturbation at the frequency f_n.

The response of the system to each freestream disturbance environment can be represented through a receptivity coefficient. The receptivity coefficient in this study $C_{rec}(f)$ is defined as the ratio of the initial amplitude of the second mode disturbance at the branch I neutral point for a given discrete frequency f to freestream forcing of the same frequency. This coefficient is determined using a combination of LST and unsteady DNS through the same process as He and Zhong.[27] This additional decomposition aims to isolate the second mode amplitudes from the complex multimodal environment induced by the transient pulse disturbance. Assuming significant second mode amplification, the receptivity coefficient can be calculated as

$$C_{rec}(f_n) = A_0(f_n) = \frac{A(s^*, f_n)}{e^{N(s^*, f_n)}}. \quad (13)$$

Here, $A(s^*, f_n)$ is the Fourier decomposed surface pressure spectral density and $e^{N(s^*, f_n)}$ is the exponentiated N-factor determined through LST for a given frequency f_n and a streamwise location s^*. The non-dimensional amplitude spectral density $A(s^*, f_n)$ for the acoustic and entropy disturbances is derived by normalizing the local surface pressure perturbation of a given frequency by the freestream pulse density perturbation of the same frequency $\rho'_\infty = |\rho'|_\infty G(f_n)$. $|\rho'|_\infty$ is the peak density perturbation amplitude defined in the previous dispersion relations. $G(f_n)$ is the analytical frequency domain representation of the incident pulse at the frequency f_n. This is given as

$$G(f_n) = \frac{\sigma\sqrt{(2\pi)}}{C_\infty} \exp\left(\frac{-2\pi^2\sigma^2 f_n^2}{C_\infty^2}\right). \quad (14)$$

The vorticity pulses are similarly normalized using the freestream velocity disturbance $v'_\infty = |v'|_\infty M_\infty G(f_n)$, since density disturbances are not imposed in the freestream. The normalizations are based on the relative peak amplitude ϵM_∞ from the dispersion relations given in Sec. III C and account for the non-uniform frequency distribution of disturbance amplitudes in the freestream pulses.

The phase angle coefficients can also be extracted using a similar decomposition method. The corresponding phase angle coefficients at the branch I neutral point can be calculated using the following equation:

$$\phi_{n,0}(f_n) = \phi_n(s^*, f_n) - \int_{s_0^*}^{s^*} \alpha_r(s, f_n) ds. \quad (15)$$

Here, ϕ_n represents the FFT phase angle from Eq. (12) at a given frequency f_n and sampling location s^* and α_r is the LST derived spatial wavenumber at the same frequency and spatial position. This is taken from the fact that the streamwise wavenumber is defined as the streamwise gradient of the local disturbance phase angle.

IV. STEADY FLOW FIELD SOLUTION

Partial mean flow entropy contours for the cone are shown in Fig. 2, encompassing both the nose regions and a significant downstream portion of the cones for both case B and case I. In both cases, a total of 240 points were used in the η direction, while the distribution in ξ ranged from 30 points per mm at the nose to 5 points per mm at the end of the domain. These distributions were chosen to ensure that sufficiently large wavenumber disturbances could be captured by the simulation and to provide sufficient resolution in the mean flow for later LST analysis. A total of 10 080 points were used in the ξ direction to resolve case B up to 1.9 m, while 7290 points were used in the ξ direction to resolve case I up to 1.5 m. The domain lengths were chosen to ensure sufficient second mode amplification for the studied pulse disturbance cases.

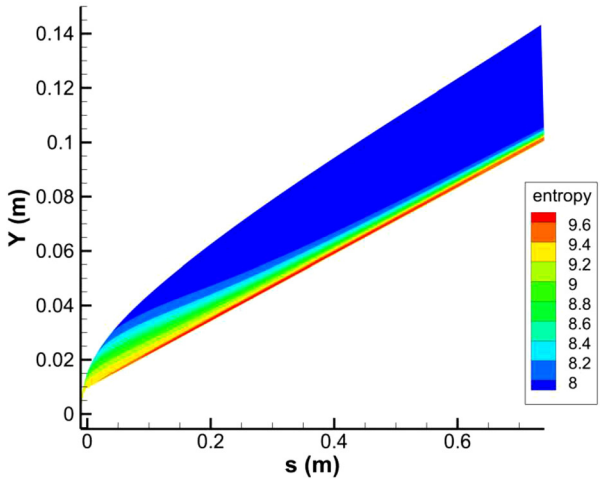

(a)

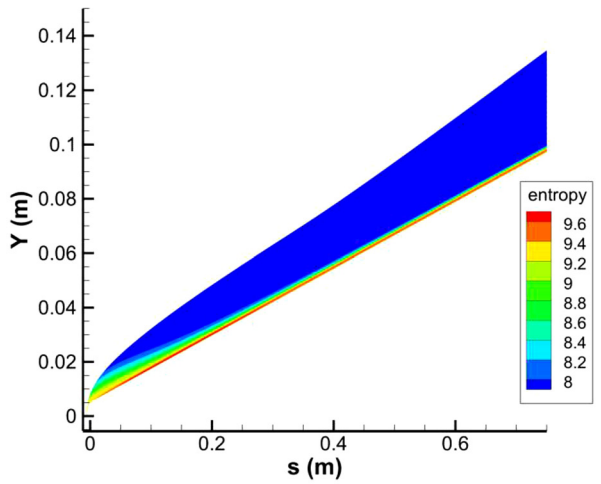

(b)

FIG. 2. Partial view of entropy contours for (a) case B and (b) case I up to 0.75 m downstream of nose.

The entropy contours for the mean flows of case B and case I in Fig. 2 depict broad entropy gradients in the frustum region immediately after the nose. These entropy gradients constitute the entropy layers generated in flows over blunt cones and are a direct result of the leading edge bluntness of the geometries. In both cases, significant gradients are observed immediately at the nose, with the entropy layer merging or being "swallowed" into the boundary layers further downstream along the cone. The larger nose bluntness for case B in Fig. 2(a) is observed to increase both the thickness of the total shock layer as well as the spatial extent of the entropy layer when compared to the sharper case I in Fig. 2(b).

The entropy and density profiles for the mean flows are plotted at different streamwise positions in Fig. 3 for case B and Fig. 4 for case I. In these figures the boundary layer and entropy layer thicknesses at specific streamwise positions can be defined as the wall-normal positions at which the parameter gradients are zero. As such, distinct entropy layers are evident in both case B in Fig. 3(b) and case I in Fig. 4(b). In both geometries, the entropy layers were observed to be swallowed approximately 100 nose radii downstream on the geometries. Additionally, the increased nose bluntness for case B is shown to greatly extend the non-parallel development of both the boundary layer and entropy layer. However, prior findings have shown that the boundary layer variation observed here has little effect on the total second mode stability profile of the mean flow in this study.[27,54]

V. LST

The growth rate contours and neutral stability curves are shown in Fig. 5 for case B and case I. LST results for case B indicate a strong amplified second mode band between frequencies of 118 kHz and 238 kHz, while for case I, the second mode band is observed to lie between approximately 135 and 300 kHz. The disturbances in case I are higher frequency than those of case B, which is expected as the blunter geometry in case B results in a larger boundary layer thickness. This leads to larger amplified wavelengths and lower amplified frequencies in case B when compared to case I.[43,50] The dimensional growth rates for case I in Fig. 5(b) are significantly higher than those of case B in Fig. 5(a) and reflect the stabilizing nature of nose bluntness on second mode disturbances as seen in prior computational studies.[24,43]

Discrete frequency growth rate data are presented for a 150 kHz disturbance for case B in Fig. 6(a) and a 200 kHz disturbance for case I in Fig. 6(b). The chosen disturbance frequencies are highly amplified and demonstrate strong amplification of the second mode disturbance. One primary difference between the two cases lies in the destabilized discrete mode. Second mode amplification begins after synchronization between the discrete mode F and mode S disturbances destabilizes one of the modes. In a large portion of stability studies over blunt cones and flat plates, the discrete mode S has generally been the destabilized mode.[13,19,22] However, it is also possible for the discrete mode F to become unstable instead.[55] The results here indicate that for

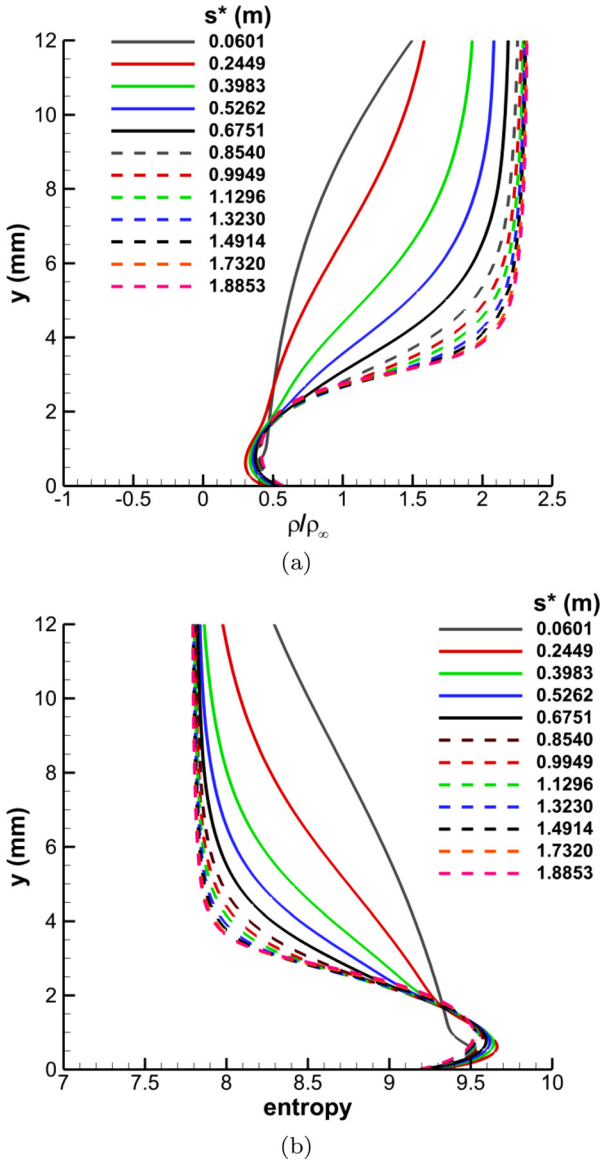

FIG. 3. Wall normal (a) density and (b) entropy profiles at different positions along the cone for case B (9.525 mm nose radius). Entropy profiles reproduced with permission from He and Zhong,[27] AIAA J. **59**, 9 (2021). Copyright 2021 Author(s).

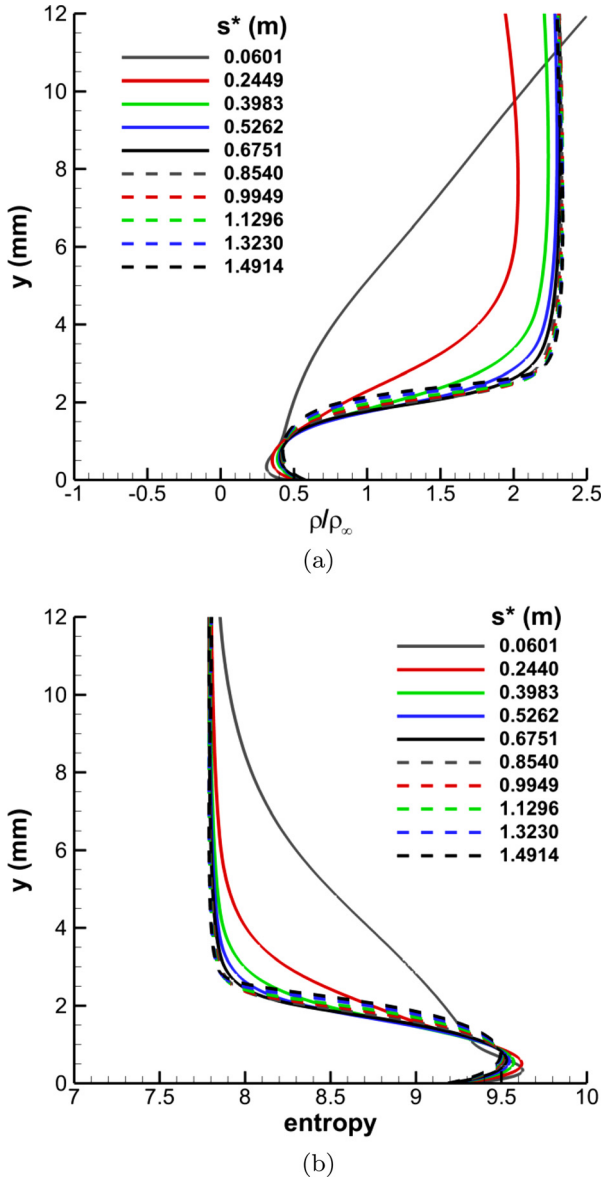

FIG. 4. Wall normal (a) density and (b) entropy profiles at different positions along the cone for case I (5.080 mm nose radius).

sharper case I, discrete mode S becomes the unstable second mode after synchronization, while discrete mode F becomes unstable for blunter case B. A prominent discontinuity is seen for discrete mode F for case I in Fig. 6(b) between $s^* = 0.5$ m and $s^* = 1$ m. The solution method of the LST code oftentimes has issues resolving the weaker discrete mode as the synchronization phenomenon creates a singularity that may be difficult to resolve numerically.[55?]

The growth rate data for a discrete frequency disturbance can be integrated in the streamwise direction using Eq. (5) to produce the N-factors for case B and case I. The resulting maximum N-factor envelope for both cases is compared against PSE derived N-factors of Marineau *et al.* in Fig. 7. For case B, which corresponds to case 3752, Marineau *et al.*[50] reported an experimental transition location of $s^* = 1.037m$ along with a transition N factor of 1.6. The LST results here predict an N-factor of 1.7 at the same point for a peak disturbance frequency of 176 kHz and are relatively consistent with Marineau's computations. Similarly for case I, which corresponds to case 3746, the experimental transition location was reported at $s^* = 0.683$ m along with a transition N-factor of 3.7. The LST analysis for this mean flow demonstrates a transition N-factor of approximately 3.9 at a disturbance frequency of 224 kHz. This peak frequency is slightly higher than Balakumar and Chou's[23] predicted 210 kHz, although this is

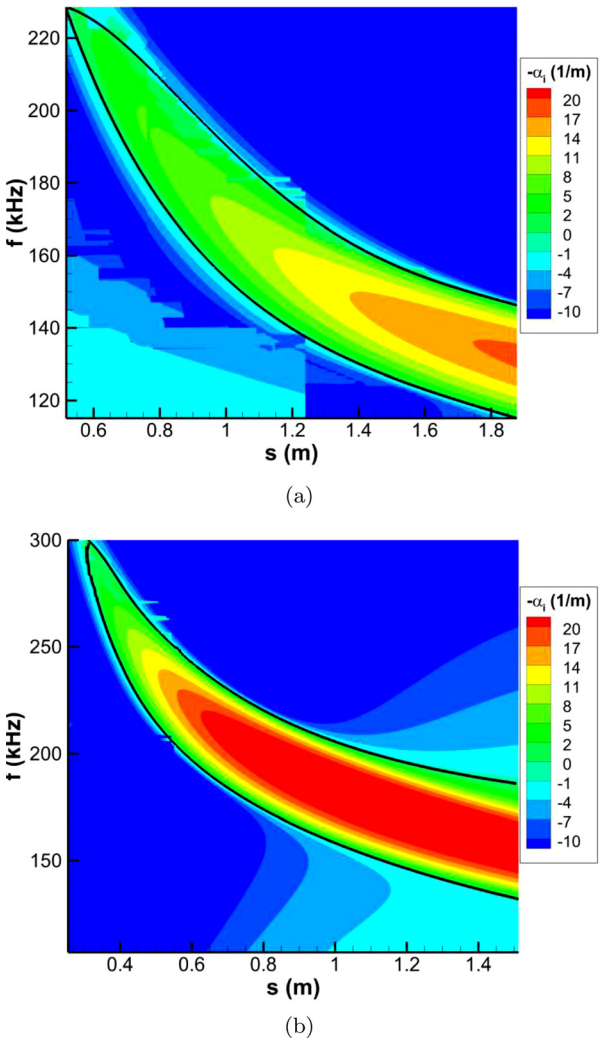

FIG. 5. Growth rate contours and neutral curves for (a) case B and (b) case I. Streamwise and frequency axes not to scale between (a) and (b). Case B results reproduced with permission from He and Zhong,[27] AIAA J. **59**, 9 (2021). Copyright 2021 Author(s).

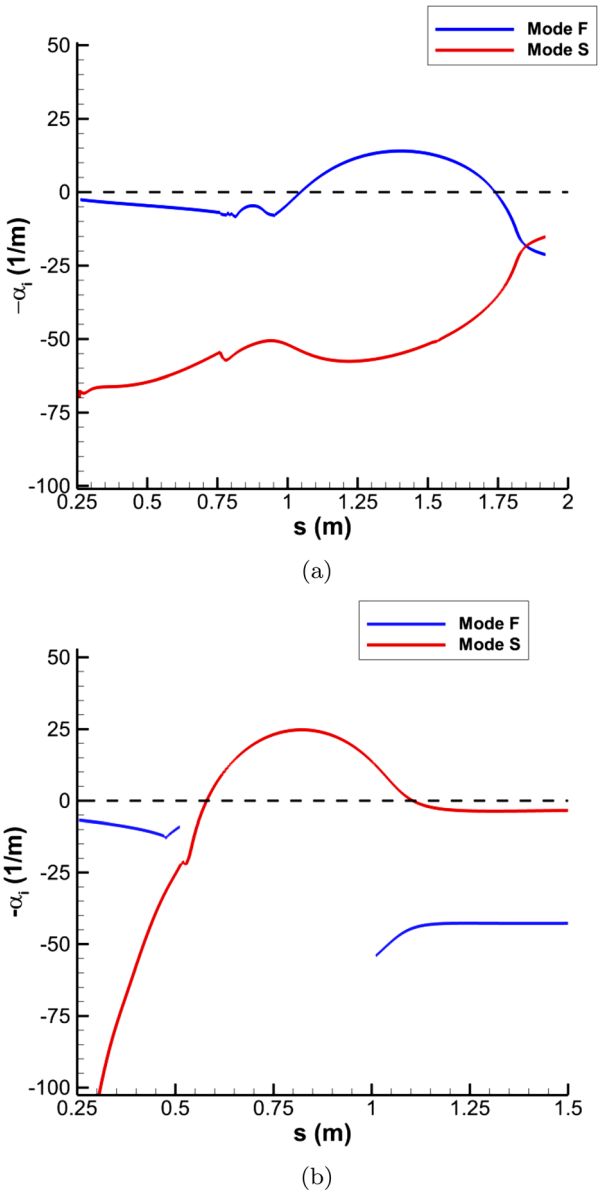

FIG. 6. Growth rate curves for specific discrete frequency disturbances (a) case B 150 kHz and (b) case I 200 kHz. Streamwise axes are not to scale between (a) and (b). Case B results reproduced with permission from He and Zhong,[27] AIAA J. **59**, 9 (2021). Copyright 2021 Author(s).

likely due to the higher unit Reynolds number for our simulation stemming from slightly different freestream viscosity models. In both cases, the LST algorithm utilized in this study seems to slightly over-predict Marineau's PSE N-factor throughout the downstream regions of the cones where the second mode is most dominant. However, this overprediction is small and is also significantly reduced in sharper Case I. This can be attributed to the weaker non-parallel effects found in sharper cone geometries. The boundary layer density profiles discussed previously in Fig. 3(a) for case B and Fig. 4(a) for case I also reflect this. The boundary layer for case I is not only observed to become parallel much further upstream in the domain, the variation between the boundary layer profiles is also seen to be much weaker than in case B. The total N-factor profiles for case B and case I are shown in Fig. 8. The larger bluntness in case B is shown to delay the onset of instabilities as well as the total amplification rate of second mode disturbances. In general, the stability analysis utilized in this study show excellent agreement with Marineau's calculated amplification factors for the tested cases.

In general, the effects of nose bluntness on the stability of the flows as measured through LST is consistent with prior findings by Lei and Zhong,[25] Kara, *et al.*,[24] and Aleksandrova *et al.*[42] Namely, the increased nose bluntness in case B is shown to directly lead to decreased second mode amplification. Spatial growth rates are shown

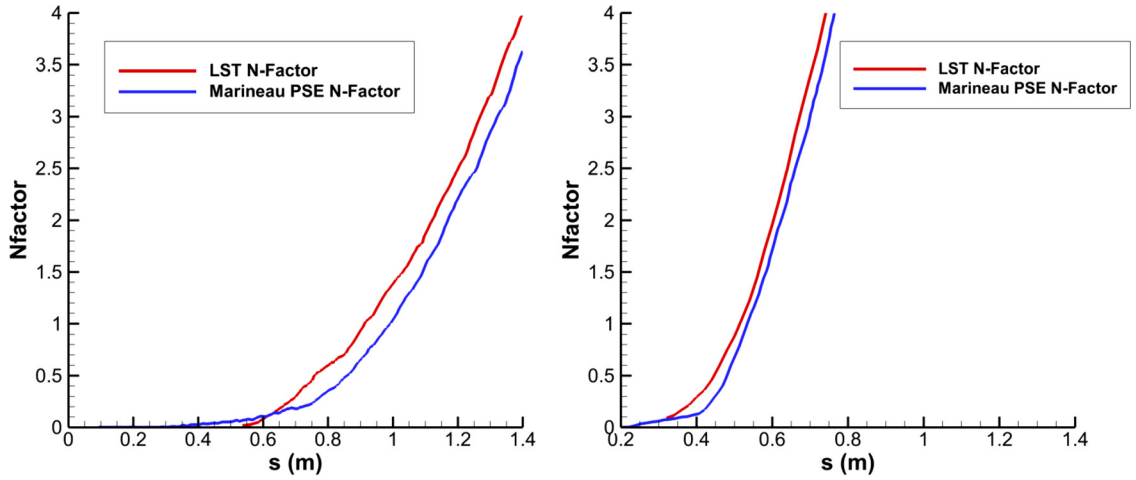

FIG. 7. Comparison of computed maximum LST N-factors against PSE N-factors of Marineau *et al.*[50] for (a) case B and (b) case I. Case B results reproduced with permission from He and Zhong,[27] AIAA J. **59**, 9 (2021). Copyright 2021 Author(s).

to be significantly lower for Case B, and the total N-factor envelopes show the expected amplification is orders of magnitude weaker. Similarly, second mode amplification is also observed to be pushed downstream in case B. The mean flow variations caused by the larger bluntness also result in a thicker boundary layer, which, in turn, amplify lower frequency disturbances.

VI. UNSTEADY DNS RESULTS

Table III provides identifying labels for the unsteady cases.

A. Finite spherical pulse results

Figure 9 depicts the instantaneous pressure disturbances immediately after the finite pulse interaction at the nose for cases B1 and I1.

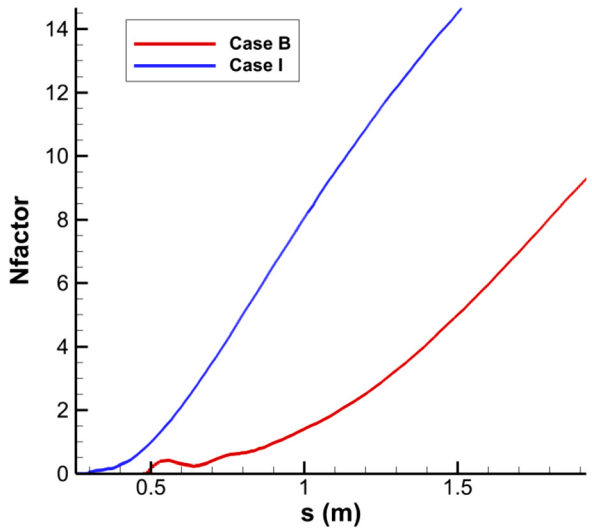

FIG. 8. Maximum N-factor profiles for case B and case I.

The pressure disturbance contours for both cases depict acoustic waves propagating toward the cone surface and being reflected back toward the bow shock in the manner expected of acoustic disturbances. Similarly, the temperature disturbance profiles at the nose are plotted again for cases B1 and I1 in Fig. 10. Instead of the acoustic reflection seen for the pressure disturbances, the temperature perturbations are seen piling up near the surface of the cone as they propagate to the end of the computational zone. This behavior reflects the emergence of excited entropy modes immediately after the bow shock.[22] Distinct differences in the spatial extent of the shock layer perturbations are observed in both the temperature and pressure disturbance contours. This is a direct result of the pulse model used, as the σ term which governs the disturbance bandwidth of the pulse also determines its spatial extent. Since this parameter was fixed between both case B and case I, the pulses remain the same size. As case I has a smaller nose radius, the resulting disturbance field is much more extensive relative to the flow field at the nose.

Figure 11 depicts shock-layer disturbance downstream on both cones for case B1 in Fig. 11(a) and for case I1 in Fig. 11(b). The other finite pulse cases were observed to demonstrate very similar

TABLE III. Freestream disturbance case labels for unsteady DNS simulations.

Disturbance type	Case B	Case I
Finite spherical fast acoustic	B1	I1
Finite spherical slow acoustic	B2	I2
Finite spherical temperature	B3	I3
Finite spherical vorticity	B4	I4
Planar fast acoustic	B5	I5
Planar slow acoustic	B6	I6
Planar temperature	B7	I7
Planar vorticity	B8	I8

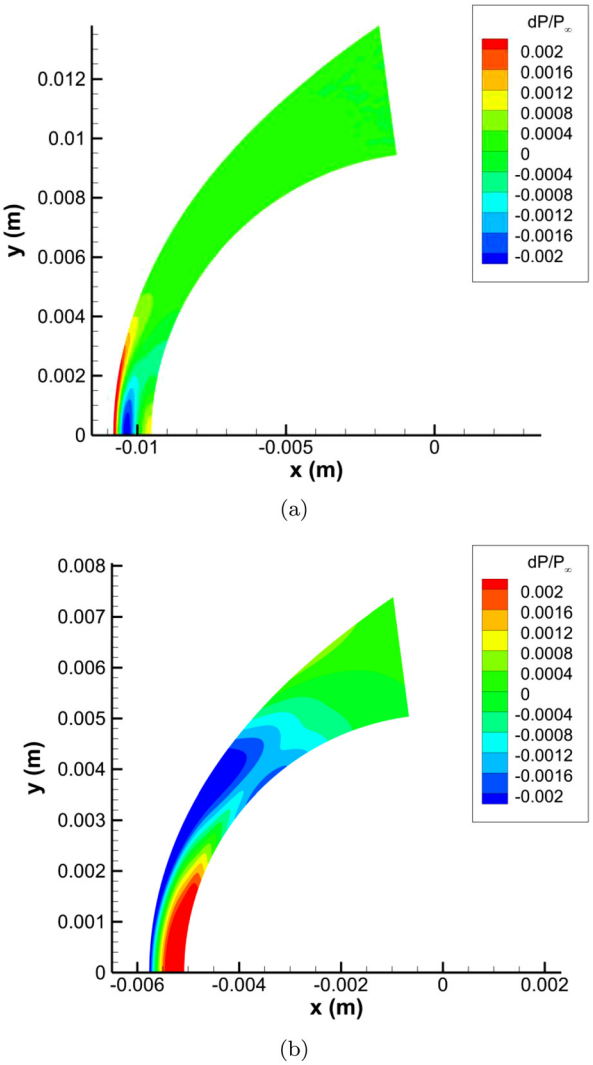

FIG. 9. Normalized pressure perturbations after finite fast acoustic pulse perturbations for (a) case B1 and (b) case I1. Axes not to scale between (a) and (b). Case B1 results reproduced with permission from He and Zhong,[27] AIAA J. **59**, 9 (2021). Copyright 2021 Author(s).

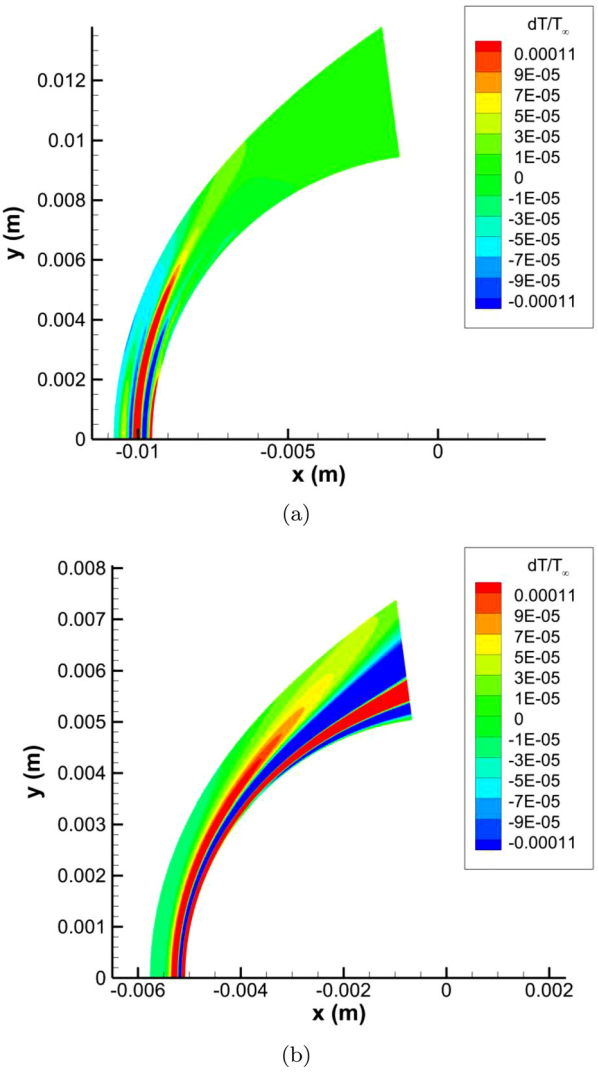

FIG. 10. Normalized temperature perturbations after finite fast acoustic pulse perturbations for (a) case B1 and (b) case I1. Axes not to scale between (a) and (b). Case B1 results reproduced with permission from He and Zhong,[27] AIAA J. **59**, 9 (2021). Copyright 2021 Author(s).

behaviors[27,54] and as such are omitted for concision. In both figures, a distinctive band of disturbances isolated near the wall surfaces can be seen and have been identified as second mode disturbances that are excited by the pulse perturbations initially introduced upstream near the nose. Additionally, structures that seem to radiate further into the shock layer are also apparent. These structures resemble Mach waves and emerge from the tail end of the second mode wave packets, between 1.25 and 1.45 m in Fig. 11(a) for case B1 and between 1.25 and 1.35 m in Fig. 11(b) for case I1. These radiative structures are the most apparent qualitative indicators of supersonic mode instabilities in the flow.[55–57] In general, these supersonic modes have been primarily studied in much higher enthalpy cases in which thermo-chemical nonequilibrium may affect the flow. Recent work, however, has also demonstrated that these supersonic modes can be found in a much wider variety of conditions including low enthalpy cases such as the mean flows in this study.[27,58] Case B1 is observed to have a distinctively stronger supersonic mode than case I1 from the larger prevalence of these Mach-wave like structures in the flow field. This was reflected in the shock-layer disturbances of each other finite disturbance case as well and indicate that much more prominent supersonic modes can be induced in case B than in case I using broadband freestream pulses. While the supersonic modes observed here are relatively weak and become apparent downstream of the experimentally determined transition locations on both cones, they provide additional sources of potential instability in the flow and merit further investigation.

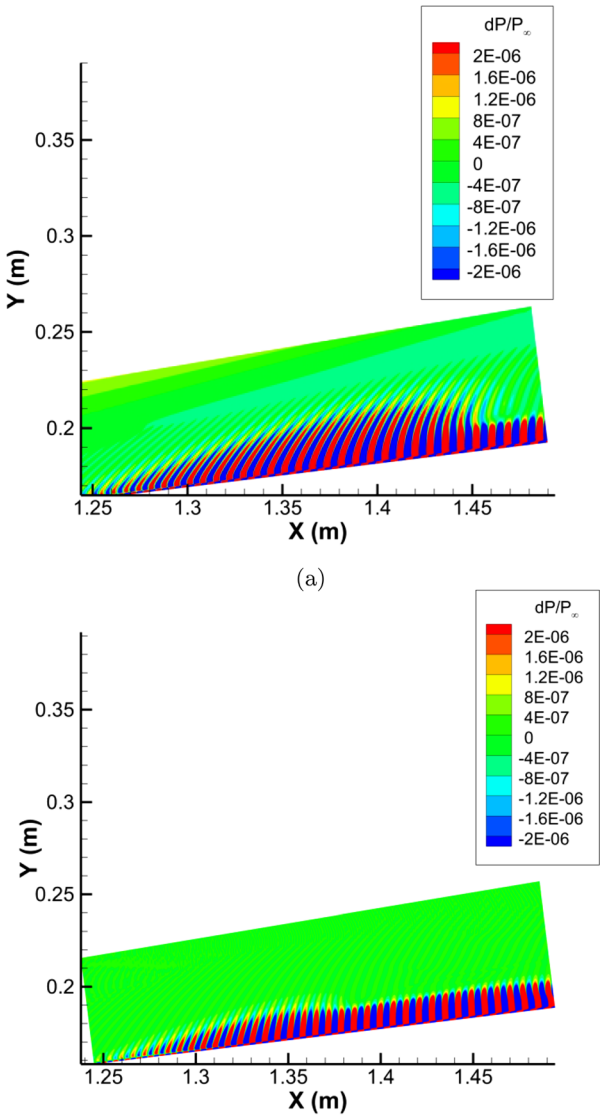

FIG. 11. (a) Case B1 and (b) case I1 pressure disturbances near s = 1.5 m after the finite spherical fast acoustic perturbation. Disturbance levels are corrected to account for differing peak freestream pulse amplitudes between cases. Case B1 results reproduced with permission from He and Zhong,[27] AIAA J. **59**, 9 (2021). Copyright 2021 Author(s).

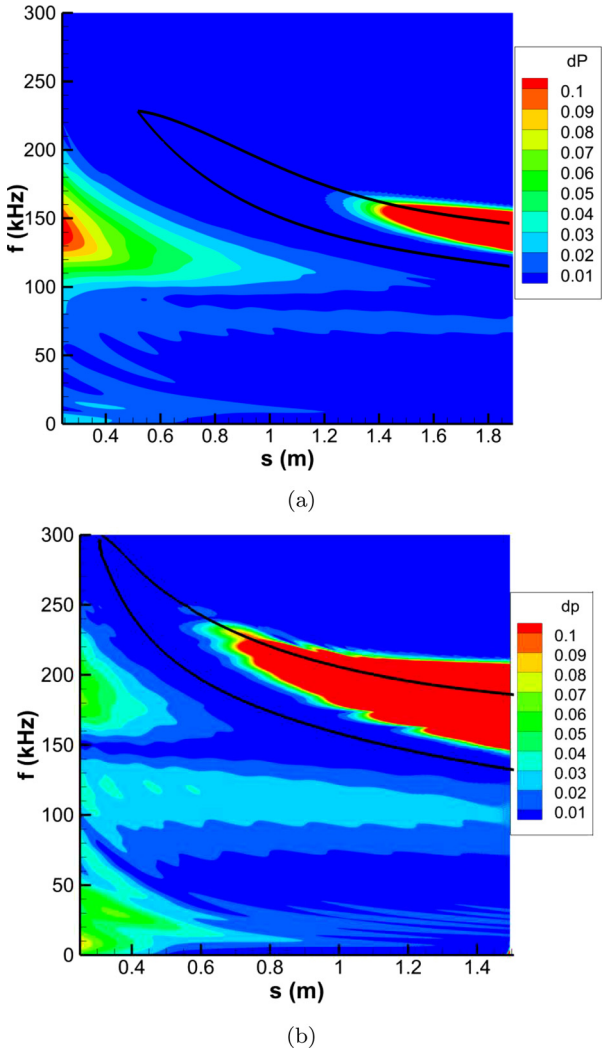

FIG. 12. Surface FFT pressure distribution for (a) case B1 and (b) case I1. Streamwise axes not to scale between (a) and (b). Case B1 results reproduced with permission from He and Zhong,[27] AIAA J. **59**, 9 (2021). Copyright 2021 Author(s).

The time history of the surface perturbations can be decomposed into their frequency components using the fast Fourier transformation (FFT). The resulting normalized spectral surface pressure contours for case B1 and case I1 are presented in Fig. 12, while the results for case B2 through B4 and cases I2 through I4 are omitted for conciseness and similarity to the presented data. Additional details for these cases can be found in He and Zhong.[27,54] The pressure disturbance contours are normalized by the spectral content of the freestream pulse to account for the non-uniform frequency distribution of the initial perturbation.[27,54] The LST neutral curves are also plotted in both figures to identify the second mode band. The general disturbance content in both of these finite pulse cases is fairly similar, with a highly amplified band of second mode disturbances centered about the branch II neutral point.[27,56] The unstable second mode region for case B1 in Fig. 12(a) occurs significantly later than for case I1 in Fig. 12(b). In particular, the LST predicts second mode destabilization at $s^* = 0.305$ m for case I and at $s^* = 0.517$ m for case B. In non-dimensional coordinates, this is approximately 55 to 60 nose radii downstream on both cones. While the second mode region begins at approximately the same downstream location in non-dimensional coordinates, the disturbance growth rates are directly observed to be higher by both LST and unsteady DNS analysis for the sharper case I.

Similar upstream forcing structures are also apparent in both finite pulse cases. Lower frequency disturbance bands are observed originating from the upstream regions, which may be attributed to other forced disturbance modes, such as continuous modes. Case B1 demonstrates weak upstream excitation of a band of disturbances between 50 and 100 kHz that experiences attenuation as it is propagated downstream. Similar, higher amplitude disturbance bands are also observed for case I1 in the frequency range between 150 and 250 kHz that is dampened immediately before the primary second mode region. Previous results from Balakumar and Kegerise[59] and Kara *et al.*[24] have shown that increasing nose bluntness also further stabilizes the first mode instability in cone geometries, which indicate that these small disturbance bands may be remnants of stable first mode disturbances that were initially excited in the non-parallel regions near the leading edges.

Additional, stronger disturbances were also observed in the finite pulse cases. For case B1, there is a large band of amplified disturbances between 100 and 200 kHz that experiences significant attenuation before the second mode region, as well as very low frequency disturbances upstream of $s^* = 0.4$ m that experience limited growth before being dampened. Again, we see similar results in case I1 with a higher frequency disturbance band between 150 and 250 kHz that is dampened as it moves downstream as well as a stronger low frequency disturbance isolated to the upstream regions of the domain. The strong higher frequency disturbances may be attributed to continuous mode instabilities excited upstream on the cone.[27] The extremely low frequency disturbances likely correspond to entropy layer instabilities excited upstream on the cone prior to the swallowing of the entropy layer and are similar to those observed previously by Wan *et al.*[26] In this case, we see that the high frequency forcing upstream on the cone is significantly stronger in the blunter case B, while the low frequency perturbations associated with entropy layer instabilities is much higher for case I.

The spatial development of surface pressure perturbation amplitudes for a selection of highly amplified second mode frequencies is given for cases B1 and I1 in Fig. 13. Upstream disturbances are again shown to experience significant attenuation until the development of destabilized boundary layer modes causes exponential disturbance growth further downstream on the cone. Case I1 demonstrates both an earlier onset of these modal instabilities, as well as higher relative disturbance amplitudes in accordance with the stronger second mode amplitudes expected in case I. The overall disturbance amplitudes immediately prior to the initial decay and amplification are also higher for case I1, though not to as noticeable an extent. This indicates a stronger relative receptivity response for case I to the finite pulse cases. The 156 kHz disturbance in case B1 also demonstrates a kink in the amplitude profile near $s^* = 1.6$ m that is not characteristic of standard second mode perturbations. The small reduction in the slope of the amplitude curve is representative of a localized increase in the growth rate for this frequency. Unstable supersonic modes have previously been shown to increase growth rates and distort and the resulting N-factor curves.[55] Such a behavior seems to be isolated to a very small range of frequencies for case B1 and is not observed in our LST analysis. This is likely due to the relatively warm walls of the mean flows in this study ($T_w/T_\infty = 1.01$), which have been shown to make supersonic modes difficult to detect with LST.[56]

B. Planar pulse results

While the finite pulses can only interact with the nose regions of the cones, the planar pulses are able to induce significantly more complex disturbance environments. Since the planar pulses are infinite in the y-z plane, they continue to interact with and perturb the shock layer as they are advected through the flow in the streamwise direction. This is demonstrated in Fig. 14 which depicts a snapshot of shock layer disturbances for case B5 and case I5. Similar structures are observed between case B5 in Fig. 14(a) and case I5 in Fig. 14(b) with a significant disturbance front observed near $s^* = 1.45$ m in both cases. This disturbance front is generated by the local interactions of the bow shock and the propagating pulse. While the general structures of the

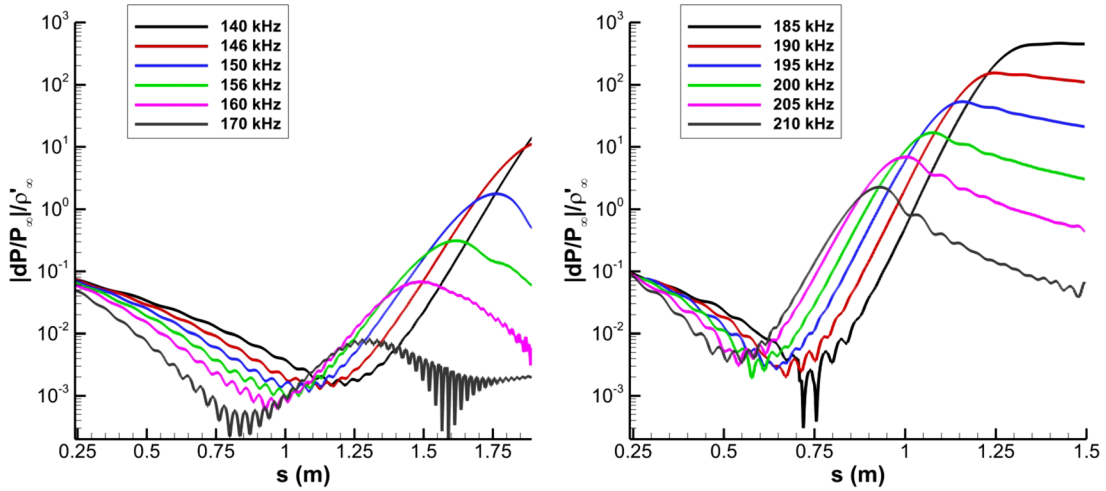

FIG. 13. Surface pressure disturbance amplitudes for selected second mode frequencies for (a) case B1 and (b) case I1. The amplitudes are normalized by the freestream pulse. Streamwise coordinate axis is not to scale between (a) and (b). Case B1 results reproduced with permission from He and Zhong,[27] AIAA J. **59**, 9 (2021). Copyright 2021 Author(s).

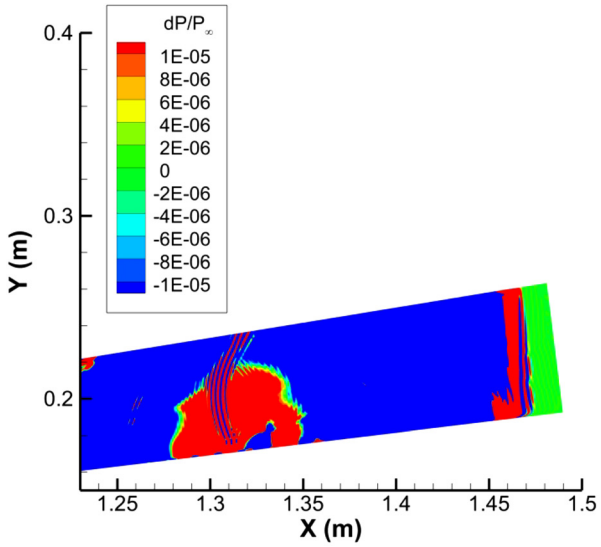

(a)

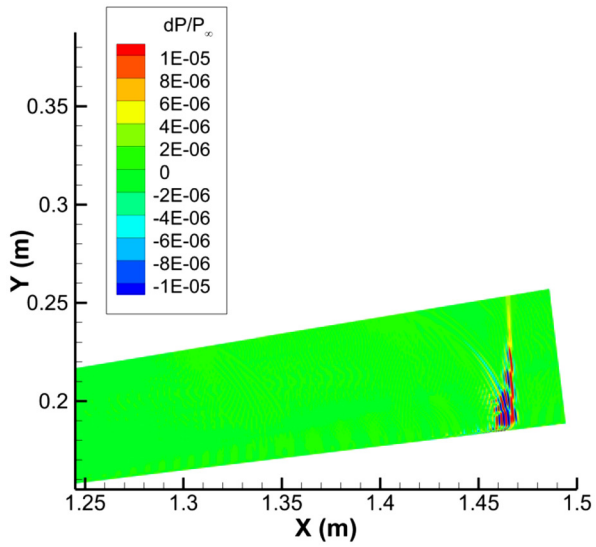

(b)

FIG. 14. (a) Case B5 and (b) case I5 planar pulse front near s = 1.5 m after the planar fast acoustic perturbation. Disturbance levels normalized to account for differences in freestream pulse strength. Case B5 results reproduced with permission from He and Zhong,[27] AIAA J. **59**, 9 (2021). Copyright 2021 Author(s).

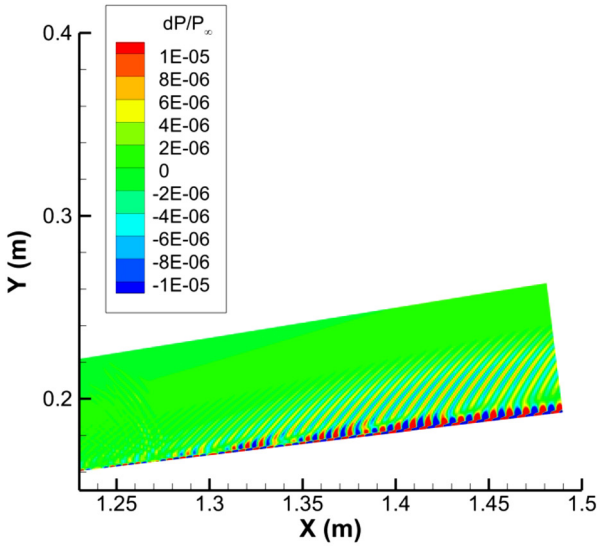

(a)

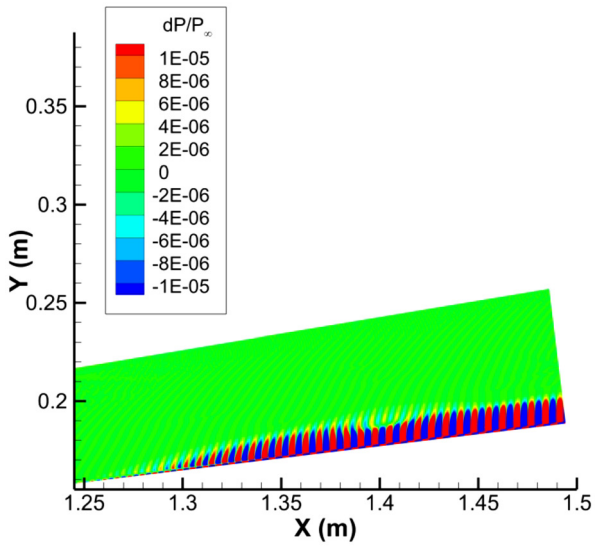

(b)

FIG. 15. (a) Case B5 and (b) case I5 second mode pressure perturbations near s = 1.5 m after the planar fast acoustic perturbation. Disturbance levels normalized to account for differences in freestream pulse strength. Case B5 results reproduced with permission from He and Zhong,[27] AIAA J. **59**, 9 (2021). Copyright 2021 Author(s).

forcing are very similar, case B5 is shown to experience much stronger disturbances throughout the shock layer than case I5. While case I5 also induces a strong pulse front that extends from the shock to the surface of the cone, these strong disturbances are isolated to the primary interaction front. Case B5, on the other hand, demonstrates strong alternating high-pressure and low-pressure disturbance regions distributed throughout the shock-layer, which is reflected in the strong non-modal forcing observed for case B5 in our later analysis. These pulse fronts and their resulting shock-layer perturbations were not observed for the other planar cases and further indicate a unique receptivity pathway downstream on cones to broadband freestream fast acoustic disturbances.[27]

These leading planar disturbance fronts are then followed by the isolated boundary layer perturbations shown in Fig. 15 for case B5 and case I5 which contain the amplified modal disturbances. The wavepacket depicted in Fig. 15(a) for case B5 demonstrates similar structures to the finite pulse cases shown previously. A clear band of

isolated, growing boundary layer disturbances is shown isolated near the wall, which are associated with the amplified second mode. Additionally, hallmark acoustic-like waves are observed radiating from these wall-bound perturbations deep into the shock layer, once again indicating the presence of a substantial supersonic mode. These are similarly reflected for case I5 in Fig. 15(b), although, in this case, the acoustic radiation is much weaker relative to the boundary layer modes. Furthermore, although amplified boundary layer modes are observed for both planar fast acoustic pulse cases, the disturbances are shown to be stronger for case I5. On the other hand, the supersonic mode is much more extensive for case B5. In general, the second mode disturbances are observed to be stronger for case I5, coinciding with LST predictions. This is reflected among all of the tested acoustic, entropy, and vorticity perturbations. Case B, however, is seen to be much more conducive to excited supersonic modes as a whole.

From the prior LST results in Fig. 6, it is seen that for case I, the discrete mode S becomes the unstable second mode after synchronization, while for case B, the discrete mode F destabilizes instead. Significant and potentially unstable supersonic modes have previously been linked to high enthalpy, cold wall flows.[56,60] Although another critical factor in determining the strength of these supersonic modes may lie in the primary boundary layer instability present in the flow, Haley and Zhong[58] showed that supersonic modes could also be observed in low enthalpy, warm wall conditions. Though, in their case, the modes were relatively weak and stable. The supersonic modes were found to originate from the stable discrete mode F instead of the destabilized mode S. The mode S phase speed generally does not fall below the phase speed of the continuous slow acoustic spectrum, which means that it is difficult for it to become supersonic relative to the mean flow. The discrete mode F, however, is much more capable of becoming supersonic in this sense.[58] Chuvakhov and Fedorov[61] and Knisely and Zhong[55,57] analyzed cases with an unstable F1 mode, similar to the Case B mean flow here. This allows for narrow bands in which the local discrete mode instability can become supersonic and unstable. These are of course more conducive to amplified supersonic mode instabilities and are a likely explanation the for the more extensive acoustic radiation observed in case B5 when compared with case I5. In general, case B saw stronger supersonic modes due to the destabilized mode F.

The FFT decomposed surface pressure contour maps for the planar fast acoustic (case B5 and case I5) and slow acoustic (case B6 and case I6) disturbances are presented in Fig. 16. The total surface disturbance spectra share many similarities to the finite spherical pulse cases. In particular, Fig. 16(c) for case B6 and Fig. 16(d) for case I6 depict upstream forcing at a band of frequencies slightly lower than the second mode frequencies predicted by LST. For case B6, these lie between 100 and 150 kHz, and for case I6, these frequencies are between 150 and 250 kHz. These disturbances are introduced upstream and experience minimal attenuation when compared to their finite pulse counterparts. This can be attributed to the continuous introduction of disturbances from the planar pulses. These upstream disturbances were found to be approximately 60% larger in case B6 when compared to case I6. The planar vorticity pulses were observed to demonstrate very similar spectral contours to the slow acoustic cases and may be found in prior work by He and Zhong.[27,54]

Additionally, the planar fast acoustic pulses in case B5 and case I5 are seen to strongly excite frequency bands outside of the primary second mode. These include coherent bands of both lower frequency and higher frequency disturbances. For case B5, these lie between 50 and 100 kHz and 170–270 kHz, while for case I5, these additional amplified bands lie between 50 and 150 kHz and 200–290 kHz respectively. From Fig. 14, we can see that the planar fast acoustic pulse induces additional shock-layer perturbations that are not observed in either the finite pulse cases or other planar pulse cases, which are likely responsible for the highly broadband surface pressure spectra observed in Figs. 16(a) and 16(b). The normalized pressure amplitude densities in these secondary instability bands remain on the same order of magnitude between case B5 and case I5, with dP peaking at approximately 12 for the lower frequency band and 23 for the higher frequency band in both cases. The second mode amplitude remains several orders of magnitude larger than these secondary bands in both planar fast acoustic cases. The similar values of these secondary bands indicates minimal variance in the receptivity of these secondary disturbances in response to the differing nose bluntnesses.

Dissimilarities were also observed for the planar temperature pulses in cases B7 and I7, which are presented in Fig. 17. Although case B7 demonstrates a more concentrated band of amplified lower frequency disturbances between 100 kHz and 200 kHz, case I7 shows a much noisier forcing environment in a manner reminiscent to the planar fast acoustic results in cases B5 and I5. In particular, a similar high frequency disturbance band is seen to be amplified between 250 kHz and 300 kHz, although it is much weaker when compared to the secondary mode in cases B5 and I5. The lower frequency band between 100 kHz and 150 kHz is also observed to not be excited. Instead, weak broadband excitation is observed throughout most of the spectrum. Additional very low frequency disturbances between 0 kHz and 30 kHz experience significant upstream excitation before they show gradual attenuation and re-amplification at the end of the cone. These likely consist of excited entropy layer modes similar to what was observed by Wan *et al.*[26] for a different cone case. These low frequency entropy layer modes were shown to be only very weakly excited by the finite pulses in both case B and case I and were demonstrated to experience only moderate excitation as a result of planar pulse disturbances in cases other than case I7. Entropy modes and entropy layer perturbations have been shown to play significant roles in the excitation of the second mode disturbance[26,28] and may be responsible for the differences in peak receptivity magnitudes observed for the temperature pulse cases in Sec. VII. These results indicate stronger entropy layer receptivity for case I, particularly in the case of freestream temperature disturbances.

The normalized surface pressure amplitude curves at a selection of second mode frequencies for the planar fast and slow acoustic pulse cases are shown in Fig. 18. Case B5 in Fig. 18(a) and case I5 in Fig. 18(b) follow similar observed trends in the finite spherical cases, with distinctive second mode amplification occurring in the expected frequency range predicted by LST. However, the second mode amplitudes for the planar fast acoustic pulses in Figs. 18(a) and Fig. 18(b) are an order of magnitude smaller than those for planar slow acoustic pulses in Figs. 18(c) and Fig. 18(d). This indicates a similar weakness of the planar fast acoustic pulse in exciting the primary second mode in both cones. Additionally, modulations in the high frequency curves are found to be much stronger in the planar fast acoustic pulse results for both cases as well. While the general profile of these disturbance amplitude curves matches the behavior expected of a second mode

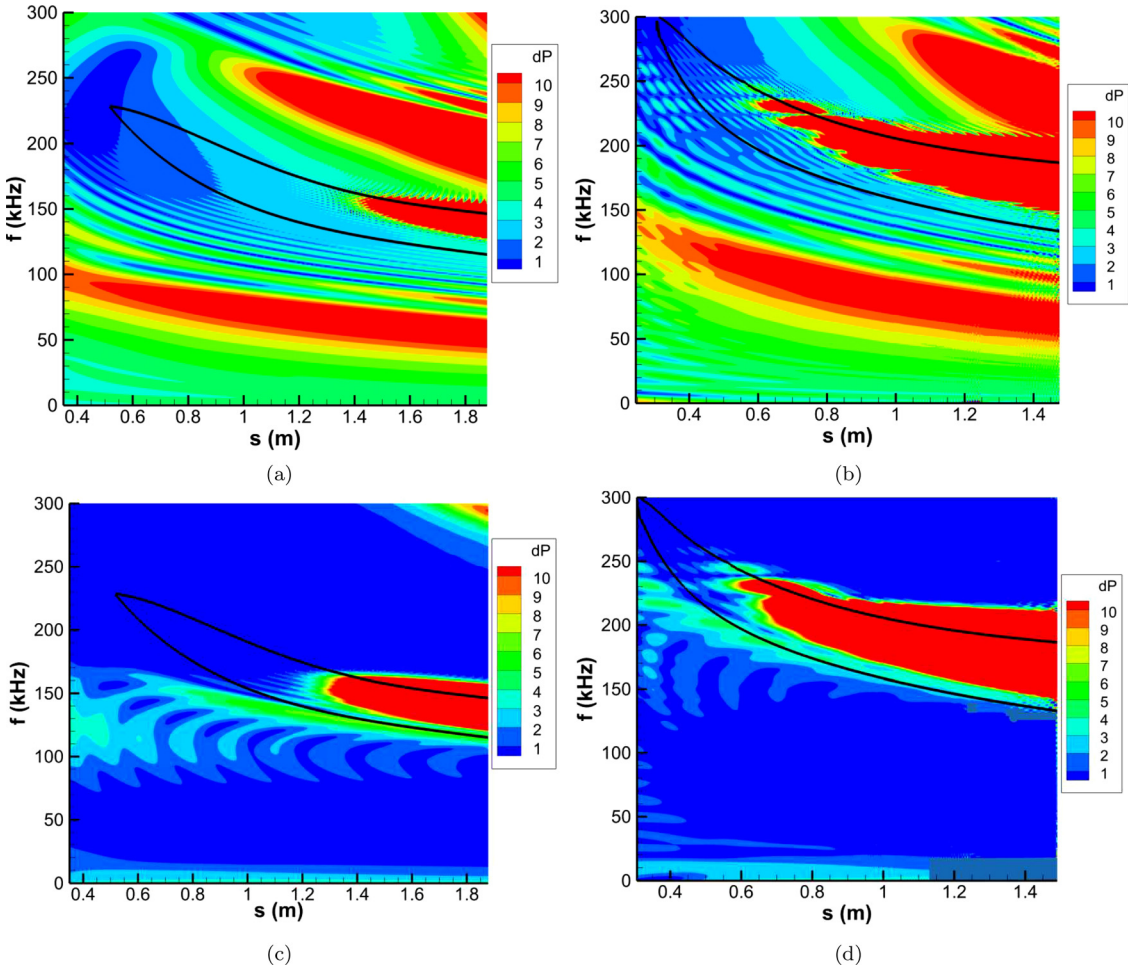

FIG. 16. Surface FFT pressure distribution for (a) case B5, (b) case I5, (c) case B6, and (d) case I6. Streamwise axes not to scale between case B and case I results. Case B results reproduced with permission from He and Zhong,[27] AIAA J. **59**, 9 (2021). Copyright 2021 Author(s).

dominated disturbance, the higher frequency perturbations, in particular, demonstrate significant levels of oscillation that are not observed for most of the planar slow acoustic results. In the 156 kHz curve in particular for case B5, the degree of these oscillations mask the region in which the localized increase in growth rate was observed for case B1. These oscillations are associated with the presence of other flow instabilities interacting with the primary disturbance.[57] While these other disturbances do not directly dominate the surface perturbation profiles, their modulation is much more significant in the higher second mode frequencies for the planar fast acoustic pulses and further indicate a strong tendency of the fast acoustic disturbance in exciting a broad range of disturbances in the flow.

C. Secondary instability bands in planar fast acoustic cases (B5 and I5)

The planar fast acoustic pulses in case B5 in Fig. 16(a) and case I5 in Fig. 16(b) denote significant amplified instability bands outside of the second mode. In order to help identify these instabilities, the pressure eigenfunction profiles for the planar fast and slow acoustic cases at a selection of frequencies are plotted for both cones. The eigenfunctions for cases B5 and B6 at the dominant second mode frequency of 153 kHz at $s^* = 1.5$ m are shown in Fig. 19. In each of these figures, the LST eigenfunctions and wall normal distance are normalized by the peak wall pressure and local shock height, respectively. The LST mode F and mode S eigenfunctions demonstrate very similar profiles, although the secondary peak of mode F is lower in amplitude. These discrete modes are clearly identifiable as their oscillations are isolated to the boundary layer.[55] The planar slow acoustic results demonstrate close adherence to the LST mode F results, which is the destabilized second mode in this case. Case B5, however, demonstrates significant deviation near the edge of and outside of the boundary layer. While the signal for case B5 initially follows closely with mode F, it eventually diverges to mode S before transitioning to become highly oscillatory outside of the boundary layer. Additionally, the eigenfunction does not decrease in amplitude, demonstrating strong excitation throughout the shock layer. These oscillations are indicative of continuous mode excitation at this frequency[55] and prior phase velocity

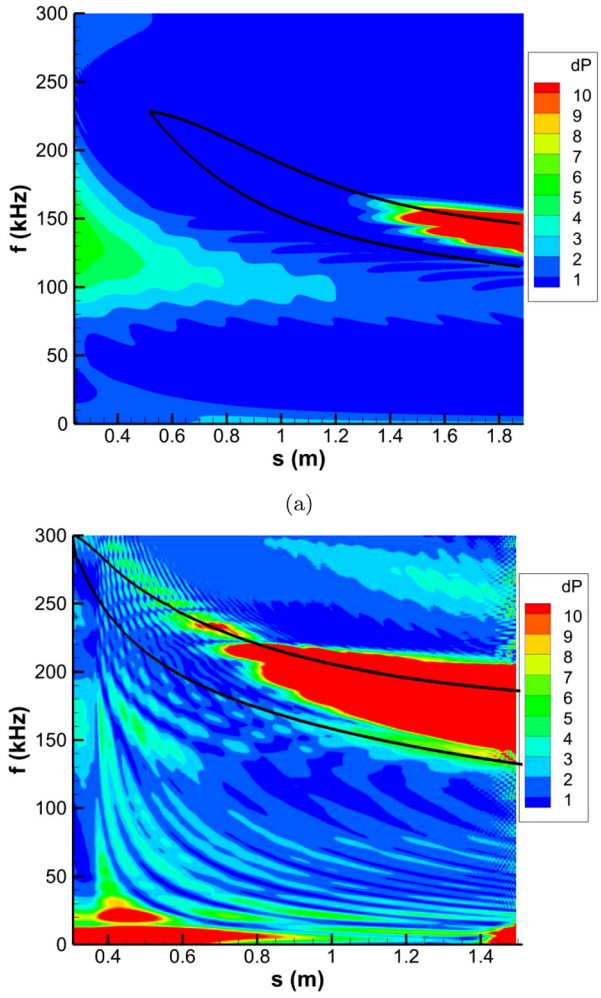

FIG. 17. Surface FFT pressure distribution contour for the planar temperature pulses in (a) case B7 and (b) case I7. Streamwise axes not to scale between (a) and (b). Case B7 results reproduced with permission from He and Zhong,[27] AIAA J. **59**, 9 (2021). Copyright 2021 Author(s).

results at a similar frequency for this case from He and Zhong[27] indicate significant excitation of continuous fast acoustic modes.

Similar eigenfunction plots are shown for the 55 kHz and 225 kHz disturbance frequencies for case B5 and case B6 in Fig. 20. Throughout these frequencies, case B5 demonstrates relatively similar behavior, with decent wall-bounded agreement inside the boundary layer followed by significant non-decaying oscillations outside of it. These behaviors again denote significant continuous mode excitation at these outer frequencies. From prior phase speed data in He and Zhong,[62] the planar fast acoustic pulse tended to more readily excite continuous fast acoustic modes at the suboptimal second mode frequencies. The case B6 results are much more variable. At 55 kHz the boundary layer portion of the eigenfunction is similar in profile to mode S but falls between mode F and mode S. This indicates potential contributions of both of these discrete modes to the DNS signal. Oscillations are also observed outside of the boundary layer for case B6, though they are more irregular throughout the shear layer. The modal content of this is hard to identify without more complex analysis tools such as multimode decomposition. Similar irregular oscillations are observed outside of the boundary layer for case B6 in the 225 kHz eigenfunctions as well. However, it should be noted that the absolute magnitude of the pressure disturbances is not equivalent between case B5 and case B6 at the three sampled frequencies. At 153 kHz, the peak pressure amplitude for case B6 is approximately an order of magnitude larger than that for case B5, while the reverse is true for the other two sampled frequencies. Additionally, the peak magnitudes for the 55 kHz and 225 kHz pressure eigenfunctions are approximately 50% smaller than the primary second mode value at 153 kHz for case B5. The peak eigenfunction values at these secondary frequencies are almost two orders of magnitude weaker than the 153 kHz value for case B6. As such, the results for case B6 at these secondary frequencies may be more sensitive to non-modal noise due to the extremely small disturbance amplitudes.

Similar eigenfunctions are plotted for case I5 and case I6 below. Figure 21 demonstrates the pressure eigenfunctions at the primary second mode frequency of 180 kHz, while Fig. 22 presents eigenfunctions at 70 kHz and 260 kHz, which correspond to the secondary bands at a streamwise position of $s^* = 1.25$ m. The primary second mode frequency results in Fig. 21 are very similar to what was observed previously for Case B at 153 kHz. Namely, excellent agreement is seen between the unsteady DNS eigenfunctions and the destabilized second mode. In this case, this corresponds to the discrete mode S. However, the planar fast acoustic pulse in case I5 is not shown to induce a significant oscillatory signal outside of the boundary layer and instead decays to 0 as expected of a dominant discrete mode disturbance. This is likely due to the stronger second mode amplification present in case I causing the destabilized discrete mode to dominate strongly over any potential continuous mode excitation. Additionally, at the 180 kHz frequency, the peak case I6 amplitude is an order of magnitude higher than that for case I5, similar to what was observed previously.

The case I5 results in Fig. 22 demonstrate very similar profiles to the eigenfunctions for case B5 in Fig. 20 at the secondary frequency lobes. When considering preliminary phase speed data from He and Zhong,[54] which also showed strong excitation of the continuous fast acoustic modes for case I5, it is likely that similar excitation patterns are present here. Namely, the planar fast acoustic pulse is introducing continuous fast acoustic modes into the flow. Since these secondary bands are outside of any regions of modal instability, they are not overshadowed like they are in the 180 kHz results. Furthermore, if the peak non-normalized pressure eigenfunction values are compared between case I5 and case B5 at the most amplified frequencies of the secondary bands, we see very similar values with dP ranging between 12 through 15.

The case I6 results demonstrate some significant differences compared to the case B6 results. Namely, agreements with the LST discrete modes is much weaker and the general oscillations are much stronger. This is particularly true for the 260 kHz results in which the case I6 eigenfunction is essentially highly oscillatory noise. The secondary frequencies at this streamwise position are well outside of the unstable second mode region and are predicted by LST to be highly attenuated. Since the planar slow acoustic pulses are not expected to induce

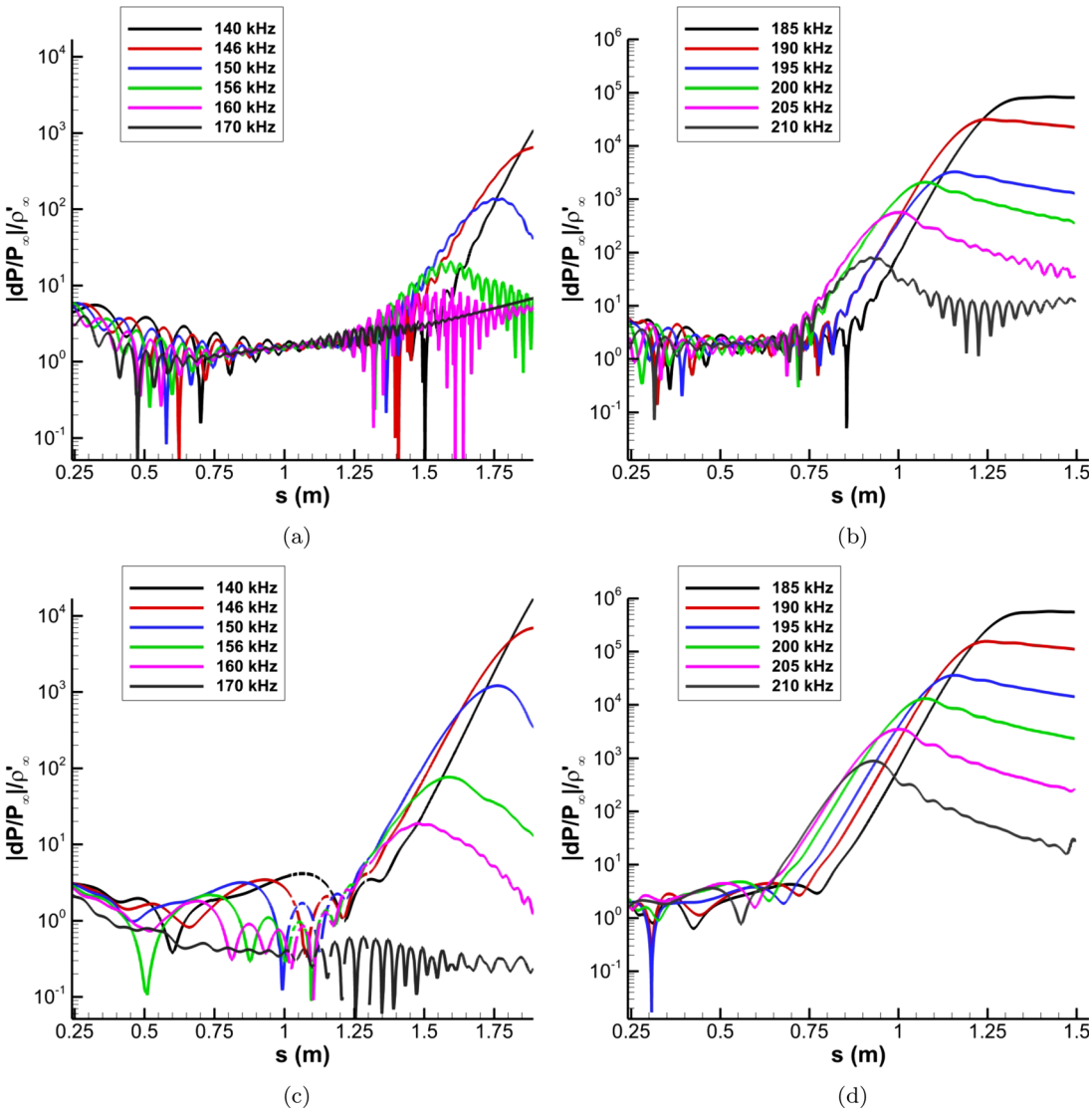

FIG. 18. Normalized surface pressure disturbance amplitudes of selected second mode frequencies for (a) case B5, (b) case I5, (c) case B6, and (d) case I6. Axes not to scale between case B and case I results. Case B results reproduced with permission from He and Zhong,[27] AIAA J. **59**, 9 (2021). Copyright 2021 Author(s).

significant continuous mode excitation,[27,54] there seems to be minimal excitation at the secondary frequencies for cases other than B5 and I5. This weak excitation may result in the increased sensitivity to non-modal noise observed here.

The similar oscillatory structures in the shear layer for the planar fast acoustic pulses indicate similar modal excitation mechanisms in both case B5 and case I5. Since continuous mode instabilities are characterized by shear layer oscillations that are not isolated to the boundary layer, it is likely that the secondary lobes found in Figs. 16(a) and 16(b) originate from excited continuous mode perturbations that are introduced throughout the flow field by the planar pulse as it propagates through the domain. Additionally, from prior phase speed analyses in Ref. 27 for case B and Ref. 54 for case I, it is likely that these lobes are composed of the continuous fast acoustic mode in particular. While the supersonic mode also induces oscillatory eigenfunctions outside of the boundary layer,[57] their effects are observed much further downstream in a very small selection of frequencies in the second mode band. As such, they are unlikely to be responsible for the secondary bands.

VII. RECEPTIVITY RESULTS

The spectral receptivity coefficient for each of the disturbances was calculated using the methodology described in Sec. III D to extract the initial second mode disturbance amplitudes at the branch I neutral point for each unstable frequency. Significant differences were observed in response to the varied nose bluntness between case B and

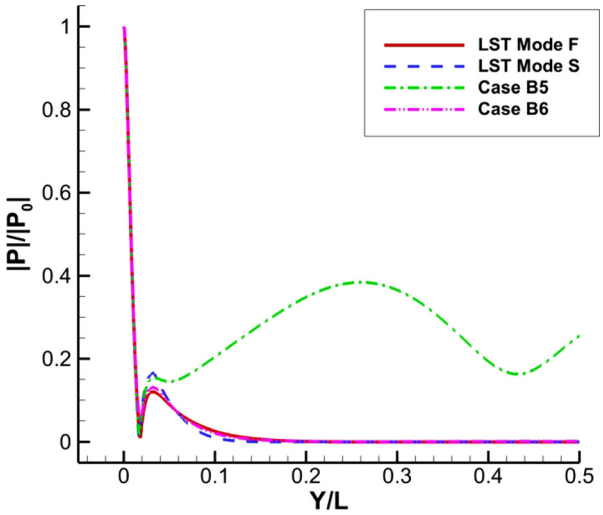

FIG. 19. Case B5 and case B6 pressure eigenfunctions at $s^* = 1.5$ m for 153 kHz disturbance.

case I. Namely, peak receptivity coefficients shift to lower frequencies in case B due to the effects of the larger nose bluntness on the mean flow. From the FFT results, it is seen that case B experiences stronger upstream excitation of moderate frequency disturbances, which are associated with excited continuous modes. Case I, however, demonstrated a stronger very low frequency response that is attributed to entropy layer disturbances. The differences in the upstream, moderate frequency forcing results in key differences in receptivity coefficients for the planar acoustic cases. The effects of nose bluntness on the receptivity process are also shown to be highly variable between the different freestream disturbance types and further confirm the complex nature of broadband receptivity in hypersonic flows.

A. Receptivity coefficient spectra

Sampling location may have a significant impact on the resultant receptivity coefficient spectra from the decomposition method utilized in this study. The effects of different disturbance sampling locations was studied for the case B unsteady pulses in He and Zhong.[27] It was found that the finite pulse results were not significantly affected by sampling location as the disturbance interactions were localized far upstream on the cone. Planar pulses, on the other hand, necessitated sampling locations further into the second mode region to more readily remove the influence of other disturbance modes in the spectra. In particular, it was found that sampling at the branch II neutral point and an intermediate sampling point defined as $x_{sample} = 1.3 * x_{brI}$, where x_{brI} is the branch I neutral stability point for the given second mode disturbance frequency would provide similar results, while branch I sampling position results are significantly impacted by the more complex forcing environment induced by the planar pulses.

A similar analysis was made in He and Zhong[54] on preliminary data for the case I unsteady pulses. While the overall receptivity spectra demonstrate prominent differences between two cone cases, they were observed to follow similar trends with regard to sampling location for both the finite and planar pulse geometries. Namely, there was little

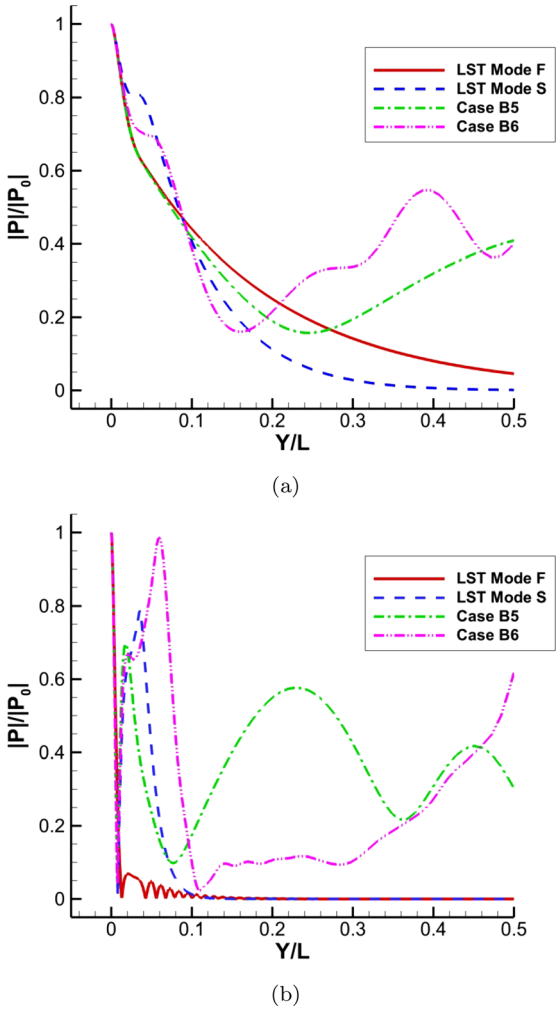

FIG. 20. Case B5 and case B6 pressure eigenfunctions at $s^* = 1.5$ m for (a) 55 kHz and (b) 225 kHz disturbance.

variation in the receptivity spectra between sampling points for the finite pulses while the planar pulses saw significant divergence only at the branch I sampling point. These are again attributed to the spatial extent of the forcing introduced by the pulses. As such, we have elected to present the coefficient results for the intermediate sampling point defined above for both case B and case I.

Figure 23 presents the total spectral receptivity coefficient results for the finite pulse cases. For case B, the finite fast acoustic pulse is observed to induce the strongest second mode response, followed by the finite temperature, slow acoustic, and vorticity pulses. The finite pulse results for case I indicate stronger receptivity responses for the temperature pulse, followed by the fast acoustic, slow acoustic, and vorticity pulses again in that order. While the general order of magnitude for most of the finite pulse cases is consistent between the mean flows for case B and case I, some distinct discrepancies in the receptivity spectra are also observed. For one, variations in the peak frequencies and amplified disturbance bands can be attributed to mean flow

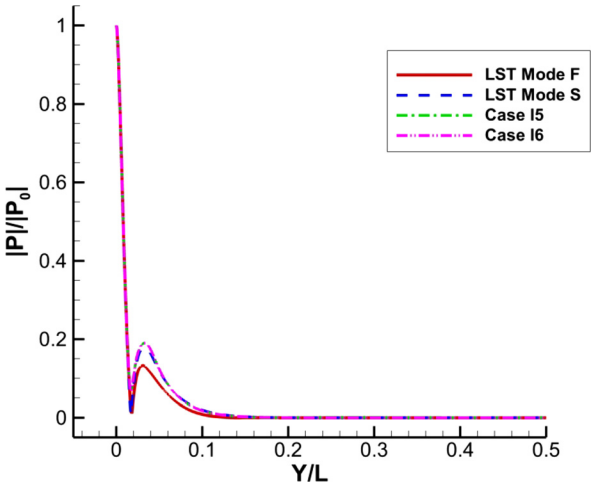

FIG. 21. Case I5 and case I6 pressure eigenfunctions at $s^* = 1.25$ m for 180 kHz disturbance.

variations caused by different nose bluntness configurations, which is also reflected in the LST results. Another primary disparity is in the overall oscillatory behavior of the spectra. As a whole, the results for cases I1–I4 demonstrate much more strongly modulated signals than for cases B1–B4, indicating stronger multimodal interactions within the boundary layer for cases I1–I4. This may be due to increased multimodal excitation upstream on the cone from the larger spatial extent of the pulse in case I. While the pulses themselves are the same bandwidth and diameter between the two cones, the sharper nose in case I causes shock–pulse interactions to occur through more of the flow field near the nose. Due to the curvature of the shock near this region, this introduces significantly more multimodal content in case I. In general, the receptivity coefficient spectra for cases I1–I4 follow the same general pattern with a peak centered around the most amplified second mode frequency.

In terms of the receptivity coefficient magnitudes, we see that the finite fast acoustic pulses in case B1 and case I1 have near equal peak amplitudes. Case B1, with a maximum disturbance near 140 kHz, has a peak receptivity coefficient of approximately 0.0031 while for case I1 has a maximum receptivity coefficient of approximately 0.0034 near 225 kHz. The finite slow acoustic and the entropy and vorticity cases are shown to have much more variable receptivity responses. For the finite slow acoustic pulses, case B2 is shown to have a peak receptivity coefficient of approximately 0.0015 while the peak receptivity coefficient of case I2 is approximately 60% larger at 0.0025. This indicates a much stronger second mode response for slow acoustic disturbances in the sharper nose case and reflects the strong receptivity response to slow acoustic disturbances observed in prior studies of cone geometries.[23]

The greatest differences in receptivity response between case B and case I for the finite pulses are observed in the vorticity and temperature disturbances. In case B, the finite temperature pulse (case B3) was observed to be of a very similar value to the slow acoustic pulse. The finite vorticity pulse (case B4) resulted in a peak receptivity coefficient of approximately $1.6E-4$, which is an order of magnitude smaller than the other pulses for case B. While the finite vorticity

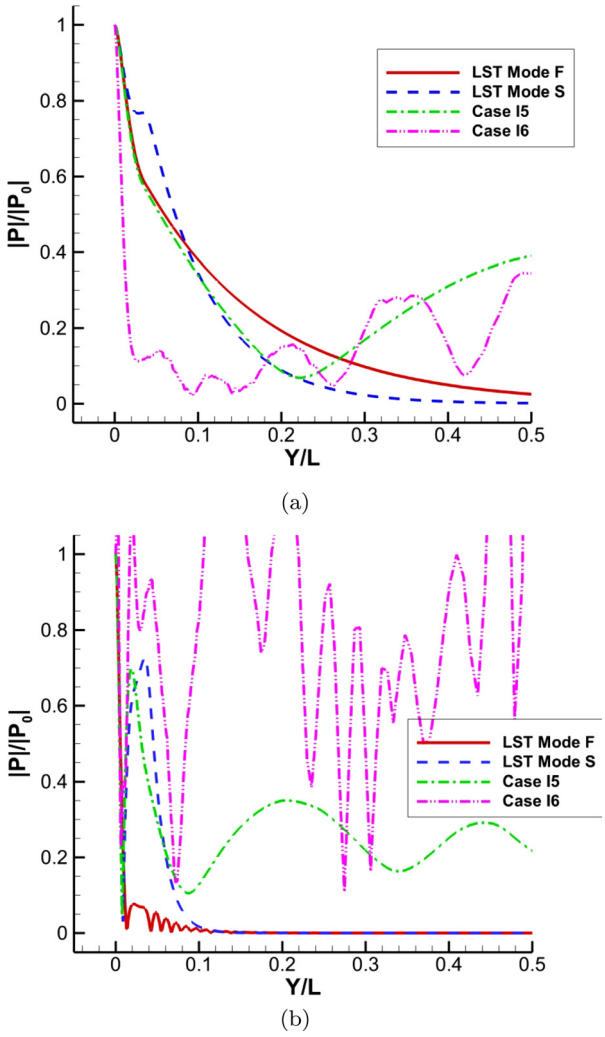

FIG. 22. Case B5 and case B6 pressure eigenfunctions at $s^* = 1.25$ m for (a) 70 kHz and (b) 260 kHz disturbance.

disturbance (case I4) also results in the weakest receptivity coefficient for case I, its amplitude is much more on par with the other cases. With a peak value of 0.0023, it is over an order of magnitude larger than its counterpart in case B. The finite temperature pulse (case I3) is also much stronger relative to the other disturbances, with it inducing the strongest second mode receptivity coefficient in the finite pulses for case I. In particular, the peak second mode receptivity coefficient of approximately 0.047 is approximately 200% larger than its counterpart in case B3, which has a peak value of approximately 0.015. These results denote a wide variance in the receptivity response between the disturbance types with regard to the nose bluntness.

The receptivity spectra for the planar pulses are plotted in a similar manner for cases B5 through B8 in Fig. 24(a) and for cases I5 through I8 in Fig. 24(b). The receptivity coefficients for the planar pulses in Fig. 24 are several orders of magnitude larger than those for the finite pulses in Fig. 23 due to different spatial extents of the

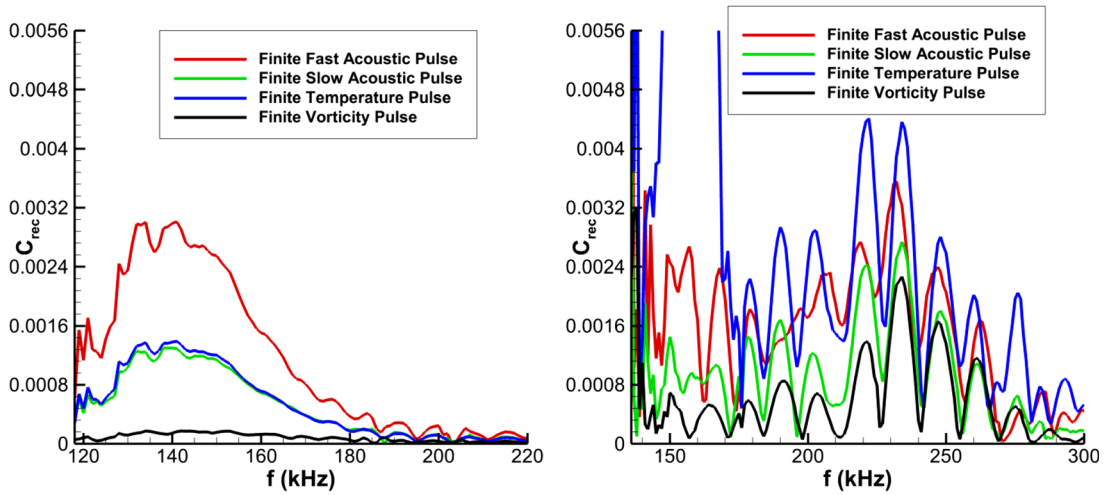

FIG. 23. Receptivity amplitude coefficient spectra for finite pulses (a) cases B1–B4 and (b) cases I1–I4. Case B results reproduced with permission from He and Zhong,[27] AIAA J. **59**, 9 (2021). Copyright 2021 Author(s).

incoming freestream disturbances. The finite pulses only interact with the cone geometries near the nose tip, while the planar pulses are infinite in the y-z plane and continue to interact with the bow shock as they are advected downstream along the cone. This additional forcing results in much higher amplitude disturbances within the shock layer relative to the strength of the freestream pulse.

The planar slow acoustic pulse dominates at lower second mode frequencies in both case B and case I. Additionally, the peak receptivity coefficient of the slow acoustic pulse in case B6 is approximately 100% larger than that for case I6, even though LST predicts stronger second mode amplification in case I. This counterintuitive behavior may be attributed to the increased receptivity of case B to instabilities outside of the standard second mode. The planar fast acoustic pulse was shown for both case B5 and case I5 in Figs. 16(a) and 16(b), respectively, to excite bands of unstable frequencies outside of the second mode, though these were orders of magnitude weaker than the primary second mode instability. The planar slow acoustic cases were similarly shown to induce significant upstream fluctuations at frequencies slightly below the second mode in Figs.16(c) and 16(c) that are attributed to local excitation in the flow by the planar pulse front. While case I6 had a much more highly amplified second mode, the lower frequency forcing upstream of the second mode region was up to 60% stronger for case B6. Prior results from He and Zhong[27] showed that significant extramodal excitation in the planar acoustic cases could cause issues with the decomposition method used here. This can be partially credited to weaker second mode amplification in case B, as the decomposition method used here requires sampling at locations of significant second mode instability to effectively extract second mode coefficients. This indicates that although the second mode in case I is more amplified, case B is more receptive to other disturbances excited by extensive broadband forcing from the freestream.

While the planar slow acoustic pulse in both cases is most dominant at the lower second mode frequencies, they are not necessarily the highest for the peak frequencies at the experimental transition locations from Marineau *et al.*[50] For case B, the peak frequency at transition is predicted to be 176 kHz, while for case I, it is 224 kHz. For case B, the planar fast acoustic pulse produces the highest receptivity coefficient at this frequency with a value of 0.78. The planar slow acoustic pulse for the same cone results in a much smaller receptivity coefficient of 0.18 at the same frequency. In case I, the planar slow acoustic pulse is strongest at the peak transition frequency and results in a peak receptivity coefficient of 1.35. This compares well to Balakumar and Chou's[23] reported case 4 receptivity coefficient of 1.2 for a discrete frequency slow acoustic wave. The increased peak frequency and receptivity coefficient of our case is likely due to differences in our freestream gas model, resulting in a higher unit Reynolds number for case I here. While the forcing regimes of these two configurations are very different, these findings reinforce that similar generalized results can be expected between continuous, discrete wave forcing and the pulses used in this study in the linear receptivity regime.

The planar fast acoustic cases demonstrate similar receptivity magnitudes, and have very similar structures. Case B5 and case I5 both demonstrate small receptivity coefficients in the lower second mode frequencies, while they gradually increase over higher frequencies instead of reaching maxima near the most amplified frequency. This behavior reflects the complex, broadband response of both flows to the planar fast acoustic pulse.[27] The peak receptivity coefficient for case B5, at a value of approximately 1.9, is 50% larger than the peak coefficient for case I5 at the higher second mode frequencies. This can again be attributed to the weaker second mode in case B. Since the secondary instabilities for the planar fast acoustic pulses were previously shown to be relatively invariant with nose bluntness, the weaker second mode in case B results in the decomposition method being less capable of removing the influence of the higher frequency noise. This is compounded by the fact that the second mode growth rates were weakest at the higher frequencies for both case I and case B.

The planar vorticity and temperature pulses are seen to have peak receptivity coefficients that are an order of magnitude larger in

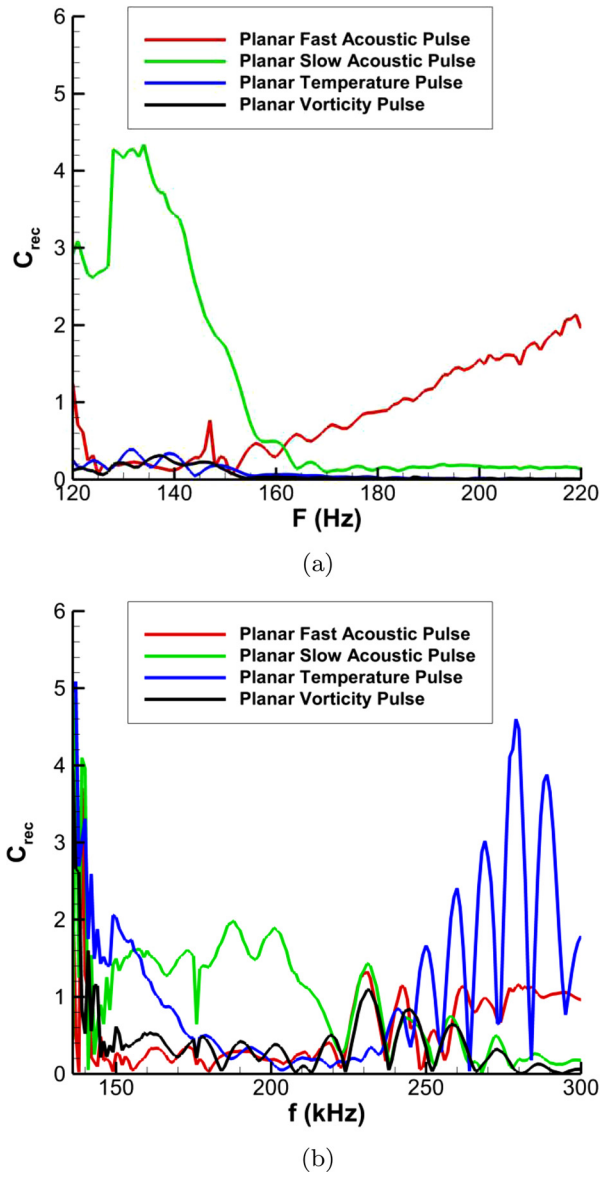

FIG. 24. Receptivity amplitude coefficient spectra for planar pulses (a) cases B5–B8 and (b) cases I5–I8. Case B results reproduced with permission from He and Zhong,[27] AIAA J. **59**, 9 (2021). Copyright 2021 Author(s).

cases I7 and I8 when compared to cases B7 and B8, similar to what was observed in the finite pulse cases previously. The stronger receptivity response for case I7 in particular, is most apparent at the extremes of the second mode frequency band. In case I, the planar temperature pulse in case I7 results in the lowest receptivity coefficient at the peak disturbance frequency, but the highest peak coefficients near 150 kHz and beyond 250 kHz. This is likely due to the excitation of nonmodal high and low frequency perturbations in a similar manner to the planar fast acoustic pulses. The stronger oscillations at these frequencies can also be traced to the noisier response seen in the disturbance spectra for case I7 in Fig. 17(b). The spectral fluctuations for this case appear to cause issues with the receptivity decomposition at the highest and lowest frequencies of the second mode band in case I7 in particular, similar to what was observed for the planar fast acoustic pulses.

B. Disturbance phase angle spectra

The phase angles of the disturbances can also be extracted from the FFT decomposition. Using a combination of the receptivity coefficient spectra and the phase angle spectra, the initial receptivity response of the flows to an arbitrary axisymmetric freestream disturbance can be reconstructed.[22,25,27] These initial disturbances can then be used to define initial perturbation conditions for more advanced transition predicted methods like Mack's amplitude method,[63] which most recently have seen development by Marineau[11] and Fedorov and Tumin.[10] Another application for these data is in the construction of arbitrary unsteady inlets for simulations studying phenomena such as nonlinear breakdown.[25,64] The receptivity phase angle spectra for the unsteady simulations is given in Fig. 25 for the finite spherical pulses in cases B1–B4 and I1–I4, while Fig. 26 presents the results for the planar disturbances in cases B5–B8 and I5–I8.

In terms of the finite pulses, strong agreement is observed between the acoustic and temperature pulses for case B. The finite vorticity pulse, however, shows substantial divergence from the other spectra at the lower second mode frequencies before converging to the other pulses at higher frequencies. Similar behavior is observed for the finite pulses in case I, though the agreement is strongest between the acoustic and vorticity pulses instead here. These three disturbances induce similar low frequency spikes in the phase spectra as observed for the finite vorticity pulse in case B, while the finite temperature pulse retains the same continuous spectra as its counterpart in case B. These large low frequency gradients in the spectra are attributed to the influence of excited extramodal disturbances in the boundary layer, and roughly coincide in frequency to the upstream disturbance bands in Fig. 12. These upstream modes contain a combination of continuous mode instabilities, as well as potentially nonmodal instabilities that greatly complicate the disturbance profile in the flow, reflecting in the sharp variations in the spectral phase profile. This forcing was previously found to be absent at the higher second mode frequencies, allowing for the convergent agreement observed here.

For the planar pulses, cases B5–B8 in Fig. 26(a) demonstrate very similar general profiles to their finite pulse counterparts. The primary difference now lies in additional offsets between the spectral phase coefficient lines that were not present for the finite pulse cases. This is due to intrinsic phase differences caused by the different freestream advection speeds of the incident disturbances.[27] This is similarly true for the planar pulse results for case I in Fig. 26(b), with another difference arising in the behavior of the planar fast acoustic pulse's phase spectra. The planar fast acoustic pulse is now seen to share much better agreement at the lower frequencies with the planar temperature pulse, contrary to large low frequency gradients observed in the corresponding finite pulse case. This is due to the different excitation mechanism observed for the planar fast acoustic pulses in general. In Fig. 16(b), it was shown that the planar fast acoustic pulse induces a much different spectral disturbance profile in the boundary layer. This includes much more distinct high and low frequency disturbance bands that are not consistent with the upstream forcing observed in the other cases. As these excited disturbances lie outside of the range of the standard

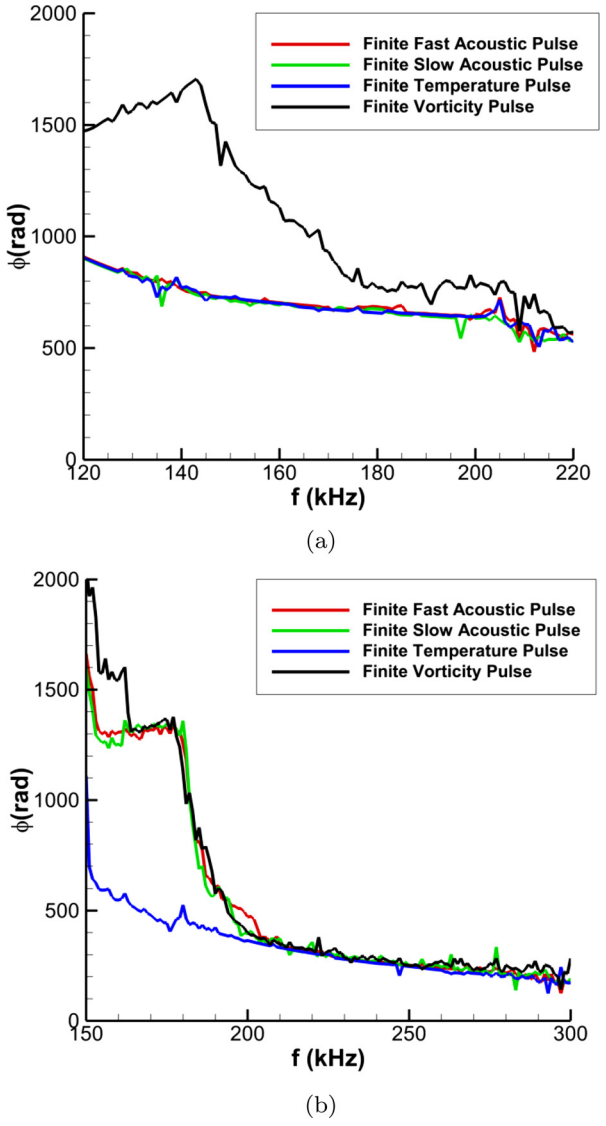

FIG. 25. Receptivity phase angle spectra after finite pulse disturbances for (a) cases B1–B4 and (b) cases I1–I4. Frequency axes not to scale between (a) and (b). Case B results reproduced with permission from He and Zhong,[27] AIAA J. **59**, 9 (2021). Copyright 2021 Author(s).

second mode, either because they are too low frequency or occur downstream of the second mode region, they do not affect the spectral phase profile. In general the differences in the extramodal excitation between the two cones causes substantial differences in the overall low frequency distribution of the phase spectra, though the high frequency behavior is very similar.

VIII. DISCUSSION AND CONCLUSIONS

In this study, we investigate the receptivity of two blunt cones of differing nose radii to freestream pulse disturbances with broadband frequency spectra. These pulses consist of acoustic, temperature, and vorticity disturbances, which are advected by the freestream velocity. Two pulse geometries were utilized: a finite pulse that forces the cones only near the leading edge and a planar geometry that also introduces forcing downstream along the cones as it propagates through the domain. Using a combination of the unsteady DNS results and stability profiles derived from LST analysis, the spectral second mode receptivity coefficients and the corresponding disturbance phase angles of the two cones were calculated and compared.

While this study is primarily concerned with the receptivity of the second mode instability, some observations were made about the impact of nose bluntness on the development of other instabilities, like the supersonic mode. Recent investigations of the supersonic mode have primarily focused on high enthalpy flows.[55–57,60] However, it has been shown that supersonic modes can also exist in low enthalpy flows with warm walls. Though the supersonic modes in these cases can be very weak and easily damped out,[58] excited supersonic modes were observed in all of the unsteady cases here. The supersonic modes are shown to be stronger relative to the second mode for the blunter cone in case B, as illustrated by the larger extent of the characteristic acoustic radiation emanating from the boundary layer disturbances in Figs. 11 and 15. This is attributed to the destabilized discrete mode F for case B, which is more likely than the discrete mode S to have its phase speed cross that of the continuous slow acoustic spectrum and become supersonic relative to the mean flow. Thus, an unstable mode F can potentially allow for stronger, unstable supersonic modes which can destabilize independently of the second mode. A variety of flow conditions govern which one of the discrete modes eventually destabilizes into the second mode, but the relatively uniform freestream and boundary conditions between these cases indicates some dependence on nose bluntness.[65]

For the finite pulses, the receptivity to fast acoustic disturbances appears to be relatively agnostic to nose radius while slow acoustic disturbances experience noticeable amplification with sharper nose geometries. Specifically, case I2 is shown to have a 60% larger peak receptivity coefficient when compared to case B2. More significant variations are observed for the finite temperature and vorticity pulses. The receptivity coefficients for the finite temperature pulse case I3 was observed to be approximately three times that of it is counterpart in case B3, while the finite vorticity pulse in case I4 was an order of magnitude larger than its counterpart in case B4.

Similar behaviors were observed for the planar temperature and vorticity results, with the receptivity coefficients for these being significantly higher in case I. However, the opposite was true for the planar acoustic disturbances. The receptivity spectra for the planar fast acoustic pulses had very similar profiles, with low amplitude receptivity coefficients at the lower second mode frequencies followed by gradually increasing higher frequency disturbances. However, the peak values for the planar fast acoustic disturbance were 50% higher for case B5 compared to case I5. This is due to the weaker second mode amplification predicted by LST for case B while similar excitation was found in the instabilities outside of the second mode. The decomposition method utilized in this study filters out less of the high frequency extramodal contribution due to the weaker second mode growth in case B. Additionally, for the planar slow acoustic pulses peak receptivity coefficients for case B6 were almost twice as high as for case I6. This is somewhat counterintuitive considering the higher second mode amplification predicted for sharper case I but can be explained through the stronger excitation of lower frequency extramodal

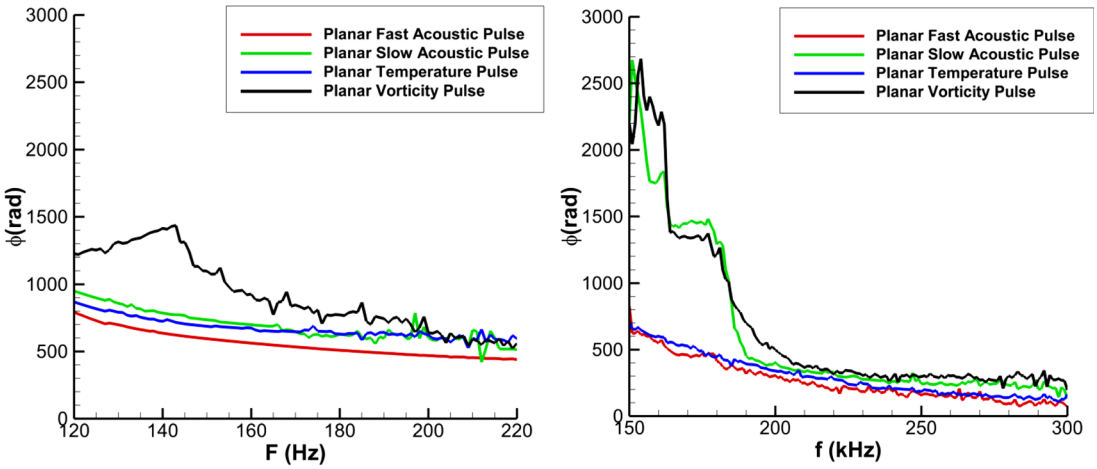

FIG. 26. Receptivity phase angle spectra after planar pulse disturbances for (a) cases B5–B8 and (b) cases I5–I8. Frequency axes not to scale between (a) and (b). Case B results reproduced with permission from He and Zhong,[27] AIAA J. **59**, 9 (2021). Copyright 2021 Author(s).

disturbances observed in the unsteady DNS for case B6 when compared to case I6. These extramodal perturbations originate upstream on the cone and are not dampened before second mode amplification begins in the planar slow acoustic cases. Additionally, even though second mode amplification gradually dominates in the appropriate band and streamwise range, this lower frequency noise is continuously introduced by local shock–pulse interactions.

The planar temperature pulse was also shown to induce a much noisier broadband spectral response in case I7 than in case B7 and demonstrated disturbance content that was somewhat similar to what was observed for the planar fast acoustic cases. This contributes to the highly modulated, multimodal receptivity spectra predicted for this case. The temperature disturbances were seen to excite much stronger low frequency disturbances associated with entropy layer modes in case I, which have been shown to be important in exciting primary disturbances downstream along the cone the in recent work by Wan *et al.*[26] and Chen *et al.*[28] This may be responsible for the much stronger temperature pulse receptivity response in case I. These entropy layer modes may also be important in the transition reversal phenomenon observed in much blunter geometries, as seen in work by Goparaju *et al.*[18] and Paredes *et al.*[49] The planar vorticity pulse is shown again to be an order of magnitude larger in case I with little variation from the behavior shown by the finite vorticity pulse case.

Overall, nose bluntness was observed to have significant effects on the receptivity behavior of the studied blunt cones to freestream pulse disturbances. The degree of this variation is dependent on the incident pulse geometry and disturbance type. Similar to prior studies, LST shows that larger bluntness attenuates the primary second mode instability by reducing the growth rate and pushing the unstable second mode region further downstream. Additionally, the larger nose bluntness in case B is seen to shift both the unstable second mode band and the frequency of the peak receptivity coefficients to lower frequencies. This is due to the thicker boundary layer that forms over the blunter geometry, which, in turn, amplifies higher wavelength and lower frequency disturbances. Differences in extramodal disturbance content were also observed. For one, supersonic modes characterized by acoustic radiation emanating from the boundary layer are shown to be more prevalent in case B due to the destabilized discrete mode F. Case B also generally demonstrated higher upstream forcing amplitudes prior to the second mode region, which consists of stronger continuous mode as well as potential nonmodal instabilities. The impact of these extramodal disturbances is reflected in the spectral receptivity coefficient and phase angle profiles. Though acoustic disturbances still resulted in the strongest receptivity response for both cones, the temperature and vorticity pulses saw a much greater relative increase in case I. This may be influenced by the stronger low frequency entropy layer disturbances observed in case I, which have been linked to second mode excitation. The acoustic disturbance coefficients, however, were generally much less sensitive relative to the changes in nose bluntness. The results demonstrate significant complexity in the receptivity response of the flow fields, which likely require additional, more advanced decomposition methods like the biorthogonal decomposition[66] to further isolate the disturbance modes of interest. Several spectral receptivity profiles, particularly for case I7, demonstrate significant oscillatory distributions that may make direct application difficult. Separating out the contribution of the primary disturbance modes of interest will be necessary to remove these spurious oscillations from the data, which can then be applied to the development of amplitude methods such as those by Mack,[63] Marineau,[11] and Fedorov and Tumin.[10] Additional efforts investigating the impacts of phase coherence as well as more complex three-dimensional disturbances will be necessary to completely characterize the receptivity of blunt cones in hypersonic flows.

ACKNOWLEDGMENTS

This research was supported by the Air Force Office of Scientific Research (AFOSR) under AFOSR Grant No. FA9550-19-1-0206, previously monitored by Dr. Ivett Leyva and currently under the supervision of Dr. Sarah H. Popkin. This work was also

partially supported by Office of Naval Research (ONR) under Grant No. N00014-17-1-2343, monitored by Dr. Eric Marineau. Primary computational resources were provided by the Extreme Science and Engineering Discovery Environment (XSEDE) through the Texas Advanced Computing Center (TACC) and the San Diego Supercomputer Center (SDSC) under Grant No. TG-ASC090076, supported in part by the National Science Foundation (NSF). Additional computational resources were provided by the Department of Defense High Performance Computing Modernization Program (DoD HPCMP) through Project No. AFOSR40702004. The views and conclusions contained herein are those of the authors and should not be interpreted as necessarily representing the official policies or endorsements, either expressed or implied, of the U.S. Air Force Office of Scientific Research, Office of Naval Research, XSEDE, or the U.S. Government.

AUTHOR DECLARATIONS

Conflict of Interest

The authors have no conflicts to disclose.

DATA AVAILABILITY

The data that support the findings of this study are available from the corresponding author upon reasonable request.

REFERENCES

[1]A. Fedorov, "Transition and stability of high-speed boundary layers," Annu. Rev. Fluid Mech. **43**, 79–95 (2011).
[2]E. Reshotko, "Hypersonic stability and transition," in *Hypersonic Flows Reentry Problems* (Springer, 1991), Vol. 1, pp. 18–34.
[3]X. Zhong and X. Wang, "Direct numerical simulation on the receptivity, instability, and transition of hypersonic boundary layers," Annu. Rev. Fluid Mech. **44**, 527–561 (2012).
[4]Y. Ma and X. Zhong, "Receptivity of a supersonic boundary layer over a flat plate. Part 3. Effects of different types of free-stream disturbances," J. Fluid Mech. **532**, 63–109 (2005).
[5]E. Reshotko and A. Tumin, "Application of transient growth theory to bypass transition," in *IUTAM Symposium on One Hundred Years of Boundary Layer Research*, edited by G. Meier and K. Sreenivasan (Springer, 2006), pp. 83–93.
[6]H. L. Reed, W. S. Saric, and D. Arnal, "Linear stability theory applied to boundary layers," Annu. Rev. Fluid Mech. **28**, 389–428 (1996).
[7]A. Tumin, "Flow instabilities and transition," in *Encyclopedia of Aerospace Engineering*, edited by R. Blockley and W. Shyy (John Wiley and Sons Ltd., Chichester, 2010), pp. 139–150.
[8]S. Schneider, "Effects of high-speed tunnel noise on laminar-turbulent transition," J. Spacecr. Rockets **38**, 323–333 (2001).
[9]L. M. Mack, "Transition and laminar instability," Technical Report No. NASA CP-153203, 1977.
[10]A. Fedorov and A. Tumin, "The Mack's amplitude method revisited," Theor. Comput. Fluid Dyn. **36**, 9–24 (2021).
[11]E. Marineau, "Prediction methodology for second-mode dominated boundary-layer transition in wind tunnels," AIAA J. **55**, 484–499 (2017).
[12]P. Balakumar and M. Malik, "Discrete modes and continuous spectra in supersonic boundary layers," J. Fluid Mech. **239**, 631–656 (1992).
[13]Y. Ma and X. Zhong, "Receptivity of a supersonic boundary layer over a flat plate. Part 1. Wave structures and interactions," J. Fluid Mech. **488**, 31–78 (2003).
[14]Y. Ma and X. Zhong, "Receptivity of a supersonic boundary layer over a flat plate. Part 2. Receptivity to freestream sound," J. Fluid Mech. **488**, 79–121 (2003).
[15]M. Malik and P. Balakumar, "Receptivity of supersonic boundary layers to acoustic disturbances," AIAA Paper No. 2005-5027, 2005.
[16]A. V. Fedorov, "Receptivity of a high-speed boundary layer to acoustic disturbances," J. Fluid Mech. **491**, 101–129 (2003).
[17]A. V. Fedorov, A. A. Ryzhov, V. G. Soudakov, and S. V. Utyuzhnikov, "Receptivity of a high-speed boundary layer to temperature spottiness," J. Fluid Mech. **722**, 533–553 (2013).
[18]H. Goparaju, S. Unnikrishnan, and D. V. Gaitonde, "Effects of nose bluntness on hypersonic boundary layer receptivity and stability," J. Spacecr. Rockets **58**, 668–684 (2021).
[19]X. Zhong and Y. Ma, "Boundary-layer receptivity of Mach 7.99 flow over a blunt cone to free-stream acoustic waves," J. Fluid Mech. **556**, 55–103 (2006).
[20]P. Balakumar and M. Kegerise, "Receptivity of hypersonic boundary layers over straight and flared cones," AIAA Paper No. 2010-1065, 2010.
[21]P. Balakumar and M. Kegerise, "Receptivity of hypersonic boundary layers to acoustic and vortical disturbances," AIAA Paper No. 2011-371, 2011.
[22]Y. Huang and X. Zhong, "Numerical study of hypersonic boundary-layer receptivity and stability with freestream hotspot perturbations," AIAA J. **52**, 2652–2672 (2014).
[23]P. Balakumar and A. Chou, "Transition prediction in hypersonic boundary layers using receptivity and freestream spectra," AIAA J. **56**, 193–2606 (2018).
[24]K. Kara, P. Balakumar, and O. Kandil, "Effects of nose bluntness on hypersonic boundary-layer receptivity and stability over cones," AIAA J. **49**, 2593–2606 (2011).
[25]J. Lei and X. Zhong, "Numerical simulation of freestream waves receptivity and breakdown in Mach 6 flow over cone," AIAA Paper No. 2013-2741, 2013.
[26]B. Wan, C. Su, and J. Chen, "Receptivity of a hypersonic blunt cone: Role of disturbances in entropy layer," AIAA J. **58**, 4047–4054 (2020).
[27]S. He and X. Zhong, "Hypersonic boundary-layer receptivity over a blunt cone to freestream pulse disturbances," AIAA J. **59**, 3546–3565 (2021).
[28]Y. Chen, G. Tu, B. Wan, C. Su, X. Yuan, and J. Chen, "Receptivity of a hypersonic flow over a blunt wedge to a slow acoustic wave," Phys. Fluids **33**, 084114 (2021).
[29]L. Duan, M. M. Choudhari, A. Chou, F. Munoz, R. Radespeil, T. Schilden, W. Schroder, E. Marineau, K. Casper, R. Chaudhry, G. Candler, K. Gray, and S. Schneider, "Characterization of freestream disturbances in conventional hypersonic wind tunnels," J. Spacecr. Rockets **56**, 357–607 (2019).
[30]X. Zhong, "Effect of nose bluntness on hypersonic boundary layer receptivity over a blunt cone," AIAA Paper No. 2005-5022, 2005.
[31]B. Wheaton, T. Juliano, D. Berridge, A. Chou, P. Gilbert, K. Casper, L. Steen, and S. Schneider, "Instability and transition measurements in the Mach-6 quiet tunnel," AIAA Paper No. 2009-3559, 2009.
[32]A. Chou, "Characterization of laser-generated perturbations and instability measurements on a flared cone," Master's thesis (Purdue University, West Lafayette, 2010).
[33]A. Chou, B. Wheaton, C. Ward, P. Gilbert, L. Steen, and S. Schneider, "Instability and transition research in a Mach-6 quiet tunnel," AIAA Paper No. 2011–0283, 2011.
[34]R. Koontz, G. Buck, and R. Kimmel, "Experimental study of spark-induced impulsive acoustic disturbances in supersonic flow," AIAA Paper No. 2002-0141, 2002.
[35]P. V. Chuvakhov, A. V. Fedorov, and A. Obraz, "Numerical modelling of supersonic boundary-layer receptivity to solid particulates," J. Fluid Mech. **859**, 949–971 (2019).
[36]O. Browne, S. Al Hasnine, and C. Brehm, "Numerical method for particulate-induced high-speed boundary layer transition simulations," AIAA J. **59**, 1196–1213 (2021).
[37]I. V. Egorov, A. V. Fedorov, A. V. Novikov, and P. V. Chuvakhov, "The role of receptivity in prediction of high-speed laminar-turbulent transition," in *IUTAM Laminar-Turbulent Transition*, edited by S. Sherwin, P. Schmid, and X. Wu (Springer International Publishing, Cham, 2022), pp. 541–552.
[38]C. Hader and H. F. Fasel, "Towards simulating natural transition in hypersonic boundary layers via random inflow disturbances," J. Fluid Mech. Rapids **847**, R3–1–14 (2018).
[39]C. Hader and H. F. Fasel, "Direct numerical simulations of hypersonic boundary-layer transition for a flared cone: Fundamental breakdown," J. Fluid Mech. **869**, 341–384 (2019).

[40]E. Softley, B. C. Graber, and R. E. Zempel, "Transition of the hypersonic boundary layer on a cone, Part II: Experiments at m = 10 and more on blunt cone transition," Technical Report No. R68SD14, 1968.
[41]K. Stetson, E. Thompson, J. Donaldson, and L. Siler, "Laminar boundary layer stability experiments on a cone at Mach 8, Part 2: Blunt cone," AIAA Paper No. 84-0006, 1984.
[42]E. Aleksandrova, A. Novikov, S. Utyuzhnikov, and A. Fedorov, "Experimental study of the laminar-turbulent transition on a blunt cone," J. Appl. Mech. Tech. Phys. **55**, 375–385 (2014).
[43]J. Lei and X. Zhong, "Linear stability analysis of nose bluntness effects on hypersonic boundary layer transition," J. Spacecr. Rockets **49**, 24–37 (2012).
[44]E. Reshotko, "Transient growth: A factor in bypass transition," Phys. Fluids **13**, 1067–1075 (2001).
[45]A. Tumin and E. Reshotko, "Spatial theory of optimal disturbances in boundary layers," Phys. Fluids **13**, 2097–2104 (2001).
[46]E. Reshotko and A. Tumin, "Role of transient growth in roughness-induced transition," AIAA J. **42**, 766–774 (2004).
[47]P. Paredes, M. M. Choudhari, F. Li, J. S. Jewell, R. L. Kimmel, E. C. Marineau, and G. Grossir, "Nose-tip bluntness effects on transition at hypersonic speeds," J. Spacecr. Rockets **56**, 369–387 (2019).
[48]P. Paredes, M. M. Choudhari, F. Li, J. S. Jewell, and R. L. Kimmel, "Nonmodal growth of traveling waves on blunt cones at hypersonic speeds," AIAA J. **57**, 4738–4749 (2019).
[49]P. Paredes, M. M. Choudhari, and F. Li, "Mechanism for frustum transition over blunt cones at hypersonic speeds," J. Fluid Mech. **894**, A22 (2020).
[50]E. Marineau, C. Moraru, D. Lewis, J. Norris, and J. Lafferty, "Mach 10 boundary-layer transition experiments on sharp and blunted cones," AIAA Paper No. 2014-3108, 2014.
[51]X. Zhong, "High-order finite-difference schemes for numerical simulation of hypersonic boundary-layer transition," J. Comput. Phys. **144**, 662–709 (1998).
[52]J. Williamson, "Low-storage Runge-Kutta schemes," J. Comput. Phys. **35**, 48–56 (1980).
[53]M. R. Malik, "Numerical methods for hypersonic boundary layer stability," J. Comput. Phys. **86**, 376–413 (1990).
[54]S. He and X. Zhong, "Numerical study of the receptivity of a blunt cone to free-stream pulse disturbances in hypersonic flow," AIAA Paper No. 2021-2887, 2021.
[55]C. P. Knisely and X. Zhong, "Sound radiation by supersonic unstable modes in hypersonic blunt cone boundary layers. I. Linear stability theory," Phys. Fluids **31**, 024103 (2019).
[56]C. P. Knisely and X. Zhong, "Significant supersonic modes and the wall temperature effect in hypersonic boundary layers," AIAA J. **57**, 1552–1566 (2019).
[57]C. P. Knisely and X. Zhong, "Sound radiation by supersonic unstable modes in hypersonic blunt cone boundary layers. II. Direct numerical simulation," Phys. Fluids **31**, 024104 (2019).
[58]C. Haley and X. Zhong, "Supersonic mode in a low-enthalpy hypersonic flow over a cone and wave packet interference," Phys. Fluids **33**, 054104 (2021).
[59]P. Balakumar and M. A. Kegerise, "Receptivity of hypersonic boundary layers over straight and flared cones," AIAA J. **53**, 2097–2109 (2015).
[60]N. P. Bitter and J. E. Shepherd, "Stability of highly cooled hypervelocity boundary layers," J. Fluid Mech. **778**, 586–620 (2015).
[61]P. V. Chuvakhov and A. V. Fedorov, "Spontaneous radiation of sound by instability of a highly cooled hypersonic boundary layer," J. Fluid Mech. **805**, 188–206 (2016).
[62]S. He and X. Zhong, "Hypersonic boundary layer receptivity over a blunt cone to freestream pulse disturbances," AIAA Paper No. 2020-2057, 2020.
[63]L. M. Mack, "Transition prediction and linear stability theory," Technical Report No. AGARD CP-224, 1977.
[64]J. Sivasubramanian and H. F. Fasel, "Direct numerical simulation of transition in a sharp cone boundary layer at Mach 6: Fundamental breakdown," J. Fluid Mech. **768**, 175–218 (2015).
[65]A. Fedorov and A. Khokhlov, "Prehistory of instability in a hypersonic boundary layer," Theor. Comput. Fluid Dyn. **14**, 359–375 (2001).
[66]A. Tumin, "Three-dimensional spatial normal modes in compressible boundary layers," J. Fluid Mech. **586**, 295–322 (2007).